SYNTHESIS AND CHARACTERIZATION OF SIO_X BY MECHANICAL MILLING FOR LITHIUM-ION BATTERY NEGATIVE ELECTRODES

by

Reid Andrew Dressler

Submitted in partial fulfilment of the requirements
for the degree of Master of Science

at

Dalhousie University
Halifax, Nova Scotia
December 2020

TABLE OF CONTENTS

LIST OF TABLES iv
LIST OF FIGURES v
ABSTRACT ix
LIST OF ABBREVIATIONS AND SYMBOLS USED x
ACKNOWLEDGMENTS xii

CHAPTER 1 INTRODUCTION 1
  1.1 Background 1
  1.2 Lithium-Ion Batteries 1
    1.2.1 Anode 3
    1.2.2 Solid Electrolyte Interphase – SEI 6
  1.3 Si and SiO Anode Development 7

CHAPTER 2 MATERIAL PREPARATION 13
  2.1 Ball Milling 13
  2.2 Shaker Mill – Spex 8000 15
  2.3 Planetary Mill 16
  2.4 Horizontal Roller Milling 17
    2.4.1 Roller Mill Modifications 21
  2.5 Attritor Milling 23
    2.5.1 Attritor Mill Modifications 26

CHAPTER 3 MATERIAL CHARACTERIZATION 29
  3.1 XRD – JD2000 29
  3.2 BET Surface area measurement 31
  3.3 Mossbauer Spectroscopy 33
  3.4 KOH Oxygen Determination Method 36
  3.5 Electrochemical Testing 45
    3.5.1 dQ/dV Analysis 46

    3.5.2 V-Q Analysis 47
    3.5.3 Cell Cycling 48

CHAPTER 4 SIO$_X$ CHARACTERIZATION 50
  4.1 Long Run data collection 50
  4.2 Targeted oxygen content milling 53

CHAPTER 5 ELECTROCHEMICAL CHARACTERIZATION 58
  5.1 Roller Mill SiO$_x$ 58
  5.2 Attritor Mill SiO$_x$ 61
  5.3 Commercial SiO - Vendor A 64
  5.4 Best Cell Comparisons 65

CHAPTER 6 CONCLUSION 69
  6.1 Summary of Results 69
  6.2 Future work 70

REFERENCES 76

LIST OF TABLES

Table 3-1: Sample data collection for a milled SiO_x sample 41

Table 3-2: KOH method verification testing 41

LIST OF FIGURES

Figure 1-1 – A simple lithium-ion battery schematic showing lithium-ion transportation and intercalation into a layered cathode material during discharge and the corresponding electrode reactions 3

Figure 1-2– Specific and volumetric capacities of anode material based on data presented by Obrovac and Chevrier [7] 5

Figure 1-3 - SEI model proposed by Peled [20] highlighting the mosaic model of solid electrolyte interphase (SEI) formation 7

Figure 1-4 – Electrode stack thickness comparison showing the advantages of using a silicon alloying electrode vs. a common graphite intercalation anode 7

Figure 1-5 – Electrode volume expansion during full lithiation based on data presented by Obrovac and Chevrier [7] 9

Figure 1-6 – Interface cluster mixture model as proposed by Hohl et al. for the composition of vapor deposited SiO [34] 11

Figure 1-7 – XRD scans detailing the composition of battery grade SiO. Red Commercial SiO spectrum shows characteristic peaks of both crystalline Si and amorphous SiO_2 12

Figure 2-1 – Mechanical alloying process as presented by Gaffet et al.[48] showing a) particle fracturing during collisions, b) particle rewelding, and c) final homogenous composition 14

Figure 2-2 – Cross sectional sketch of a vibratory milling vial showing its figure-8 like milling motion 15

Figure 2-3 – Simple diagram illustrating the motion of a planetary mill 17

Figure 2-4 – Roller mill cross sectional diagrams showing air inlet, air outlet, and flow joint from the side view, and the cascading media milling effect shown in the front view 19

Figure 2-5 – Roller mill rotational speed requirements based on the milling vial radius and media size. a) $\nu \leq \nu_c$, b) ν_c, c) $\nu \geq \nu_c$ 20

Figure 2-6 – Full roller mill setup labelled and indicated 21

Figure 2-7 – Caking deposits formed during initial roller milling trials after milling for a total of a) 250 hours, b) 2 hours 22

Figure 2-8 – Roller milling vials with attached scraper blade a)/b) Cross sectional schematics, c)/d) Photos of set up 23

Figure 2-9 – Vertical axis stirred attritor mill. Inlet airflow shown in blue and outlet flow labelled red 24

Figure 2-10 – Full attritor mill setup labeled and indicated as used on the Dalhousie Engineering campus 25

Figure 2-11 – Silicon deposits forming during dry milling trails using the HD-01 attritor Mill. Solid material deposits forming on, a) Lower attritor can corners, b) Attritor can walls 27

Figure 2-12 – Attritor wet milling transformation. a) Cross sectional diagram during dry milling under gas flow. b) Cross sectional diagram during wet milling in solvent 28

Figure 3-1 – Illustration of Bragg's law showing reflection of x-rays between parallel atomic planes 29

Figure 3-2 – Micromeritics Flowsorb II 2300 gas flow schematic and separate sample degas connections 32

Figure 3-3 – Sample data of ball milled silicon powders as presented by Scott et al [69] showing an increase in $FeSi_2$ peak intensity after milling 36

Figure 3-4 - Free body diagram of a pouch bag undergoing Archimedes gas volume measurements 37

Figure 3-5 – Four step process implementing the KOH oxygen determination method ... 39

Figure 3-6 – a) Unreacted pouch bag with KOH and SiOx materials separated, b) Reacted pouch bag measuring hydrogen gas evolution 40

Figure 3-7 – Periodic SiO_x sampling and testing by the KOH method shows less H_2 is produced as more SiO_2 is formed while ball milling 43

Figure 3-8 – Quantitative oxygen content determination by the KOH pouch bag method showing a steady increase in oxygen content 43

Figure 3-9 – KOH pouch bag deterioration due to reaction between pouch bag aluminum and KOH solution 44

Figure 3-10 - Lithium electrode half cell configuration and assembly order as used in electrochemical testing 46

Figure 3-11– dQ/dV sample data for a commercial SiO electrode 47

Figure 3-12 – V-Q sample data for a commercial SiO electrode......48

Figure 3-13 – Capacity vs cycle sample data for a commercial SiO electrode......49

Figure 4-1 - Time dependant XRD patterns of samples taken from, a) Roller Mill and b) Attritor mill showing the effect of total milling time......51

Figure 4-2 - Oxygen content of ball milled silicon samples taken from a) Roller Mill and b) Attritor mill found using the KOH oxygen determination method......52

Figure 4-3 – Evidence of attritor arm wear causing unwanted Fe contamination in the SiO_x powders......53

Figure 4-4 - Oxygen content of ball milled silicon as part of targeted oxygen content milling, measured by the KOH method. Samples from a) Roller Mill and b) Attritor mill......54

Figure 4-5 – Time dependant XRD patterns of samples taken from, a) Roller mill and b) Attritor mill......55

Figure 4-6 - Time dependant BET surface area of samples taken from, a) Roller mill and b) Attritor mill showing the dramatic increase in surface area during milling......56

Figure 4-7 - SEM images of a) Silicon starting material, b) Vendor A SiO, c) Roller Mill SiO_x, and d) Attritor Mill SiO_x, comparing particle size and surface morphology......57

Figure 5-1 – Benchtop SEM images showing the effectiveness of SWCNT as a binder strengthener in increasing additive amounts of a) 0%, b) 0.08%, c) 0.15%, reducing crack size and length......58

Figure 5-2 – Roller Mill SiO_x cycle life over 50 cycles with varying SWCNT additive......60

Figure 5-3 – Roller Mill SiO_x V-Q curves over 50 cycles with varying SWCNT additive......61

Figure 5-4 – Attritor Mill SiO_x cycle life over 50 cycles with varying amount of SWCNT additive......62

Figure 5-5 – Attritor Mill SiO_x V-Q curves over 50 cycles with varying SWCNT additive......63

Figure 5-6 – Vendor A SiO cycle life over 50 cycles with varying SWCNT additive......64

Figure 5-7 – Vendor A SiO V-Q curves over 50 cycles with varying SWCNT additive......65

Figure 5-8 – Best cells from milled SiO_x and commercial SiO looking at cycle life over 50 cycles 67

Figure 5-9 – Best cells from milled SiO_x and commercial SiO looking at V-Q curves over 50 cycles 68

Figure 6-1 – Si cycling data with varied amounts of SWCNT additive 74

ABSTRACT

The need for higher energy density Li-ion batteries has led to the investigation of higher energy density anode materials. Specifically, research is focused on transitioning away from intercalation materials in favor of silicon-based alloying electrodes. Silicon electrodes offer ten times the specific capacity of graphite at the cost of poor cycle life due to large volume expansions during lithiation. This poor cycle life is attempted to be improved with the introduction of SiO_x. SiO_x is composed of nano regions of Si and SiO_2 that provide a more stable microstructure to resist particle fracturing during cycling.

SiO_x is synthesized through mechanical milling as an alternative to the current production method of vapor deposition. Mechanical milling is a well-known industrial process that would easily allow large scale production to take place. Existing roller mill vials were modified to allow compressed gas to be passed into the milling chamber and provide the oxidation reaction needed. This was aided by the introduction of a stationary scraper that would prevent caked silicon deposits from forming during milling. A second method was investigated using a commercially available attritor mill. This mill was used in a wet milling configuration that used distilled water as a milling solvent. This solvent was used in two ways as it also served as the source of oxygen used to oxidize the silicon surfaces. Both synthesis methods offered full control of oxygen content through the electrochemically useful range.

The resulting materials were characterized using a variety of methods including XRD and BET surface area analysis. A method for determining oxygen contents of the SiO_x was developed in this work based on the reaction between silicon and a potassium hydroxide solution. This method was fast and effective, allowing for the development of an oxygen content versus milling time relation. Using this relation, samples with a targeted oxygen content of $x = 0.6$ were synthesized using both methods.

The final targeted oxygen content samples were assembled into coin cells and cycled against a lithium metal counter electrode. The materials exhibited excellent specific capacity of 1750-2000 mAh/g with good capacity retention over 50 cycles. Cycling was further enhanced with the addition of a SWCNT additive solution. This SWCNT solution improves electrical conductivity, improves electrode adhesion, and helps maintain electrical contact between active particles during cycling. These results were then compared directly to commercial material.

LIST OF ABBREVIATIONS AND SYMBOLS USED

BET	Brunauer-Emmet-Teller
c	Speed of Light
CB	Carbon Black
CE	Coulombic Efficiency
CMC	Carboxymethyl Cellulose
CNT	Carbon Nano Tube
d	Lattice Interplanar Spacing
DEC	Diethyl Carbonate
DMC	Dimethyl Carbonate
EC	Ethylene Carbonate
E_R	Recoil Energy
E_γ	γ-Ray Transition Energy
E_D	Doppler Shifted γ-Ray Transition Energy
f	Recoil Free Fraction
F	Force
FEC	Monofluoroethylene Carbonate
F_R	Response Factor
FWHM	Full Width at Half Maximum
g	Acceleration Due to Gravity
HRC	Rockwell Hardness Scale C
IRC	Irreversible Capacity
IS	Internal Standard
Li-ion	Lithium Ion
Li-PAA	Lithium Polyacrylate
LTO	Lithium Titanium Oxide ($Li_4Ti_5O_{12}$)
m	Mass

M	Nucleus Mass
NMC	$Li(Ni_{1-x-y}Mn_xCo_y)O_2$
PECVD	Plasma Enhanced Chemical Vapor Deposition
r	Milling Media Radius
R	Roller Mill Inner Radius
RFF	Recoil Free Fraction
RPM	Revolutions Per Minute
SEI	Solid Electrolyte Interphase
SWCNT	Single Wall Carbon Nano Tubes
t	Diffraction Peak Width
TC	Thermal Conductivity
TEM	Transmission Electron Microscopy
unk	Unknown sample
v	Velocity
V	Volume
VC	Vinylene Carbonate
w	Crystallite Size
XRD	X-Ray Diffraction
θ	X-Ray Incident Angle
λ	Wavelength
μ	Chemical Potential
ω	Planetary Mill Rotation Velocity
Ω	Planetary Mill Revolution Velocity
ν	Angular Velocity
ν_c	Critical Angular Velocity
ρ	Fluid Density

ACKNOWLEDGMENTS

I would like to thank Dr. Jeff Dahn for the opportunity to work in his lab and learn from his vast experience over the last two years, and my family for their continued support from across the country.

A special thanks goes to Simon Trussler for taking my ideas and making them happen, and for repairing everything I broke along the way. This thank you can also be extended to Kevin and John for assisting me during the times Simon could not.

I would also like to thank Michel Johnson and my fellow Dahn lab members for advice and training along the way and for the friendships that resulted.

CHAPTER 1 INTRODUCTION

1.1 BACKGROUND

The versatile performance of lithium-ion batteries has made them the clear choice for reversible energy storage. The high energy density and mid-level power characteristics of lithium-ion batteries make them suitable for applications such as stationary energy storage, electric vehicles, and personal electronic devices. Due to the greater energy density and practicality of lithium-ion batteries, they are repeatedly chosen over the existing range of lead acid, nickel metal hydride, and nickel cadmium rechargeable batteries. The lithium-ion battery's popularity is evident in all areas, with the exception of the 12 V lead-acid battery used in the internal combustion automotive industry. The intermittent nature of renewable energy capture requires batteries that can perform reliably under all charging and discharging scenarios. Batteries used in the automotive industry require a safe, high energy density, high average-voltage power source to maximize electric vehicle range. The high energy density and zero maintenance characteristics of lithium-ion batteries also make them the ideal choice for powering small electronic devices.

1.2 LITHIUM-ION BATTERIES

The operating principles of a lithium-ion battery are based on the transport of lithium ions between a positive and a negative electrode. A basic Li-ion cell consists of four basic parts: a lithium intercalation cathode, a lithium intercalation or lithium alloying anode, a microporous separator between the two electrodes, and a lithium ion conducting electrolyte. Positive electrodes and negative electrodes are colloquially referred to as cathode and anode material and may be used interchangeably in literature. Positive electrodes are typically a lithium metal oxide or phosphate compound with layers or tunnels in which to reversibly intercalate lithium ions. Negative electrodes are typically a graphite-based mixture intercalating lithium-ions between the individual graphene sheets but can also be a lithium alloying material. The microporous separator between the electrodes allows for the passage of lithium ions but prevents any short circuiting between electrodes. Electrolyte consists of an ion-conducting lithium salt such as $LiPF_6$ dissolved in a mixture of organic solvents and additives (eg: EC, DEC, DMC, VC, FEC). Lithium-ion batteries were first introduced commercially in 1991 by Sony and have grown in popularity ever since. These batteries produced by Sony consisted of a lithium cobalt oxide cathode paired with a petroleum coke anode. The voltage of a given positive-negative electrode pair can be defined in terms of the chemical potential of lithium in each of the materials as given by Equation 1.1.

$$-eV = \mu_+ - \mu_-, \qquad \text{E1.1}$$

where μ_+ and μ_- are the chemical potentials of lithium atoms contained in the positive and negative electrodes, respectively and e represents the charge of an electron.

At a full state of charge, lithium-ion batteries store lithium ions in the negative electrode. During discharge, lithium ions are transported by the electrolyte, through the separator, to be intercalated into the positive electrode. As this ion is transported though the cell, the corresponding electron is driven though an external circuit, doing work, before recombining with a lithium ion in the positive electrode. This continuous ionic charge flow results in a corresponding current through the external circuit that will be sustained until the battery is fully discharged. The reactions describing the operation are given in the following reactions as part of Figure 1.1 where it is assumed that silicon is the negative electrode material.

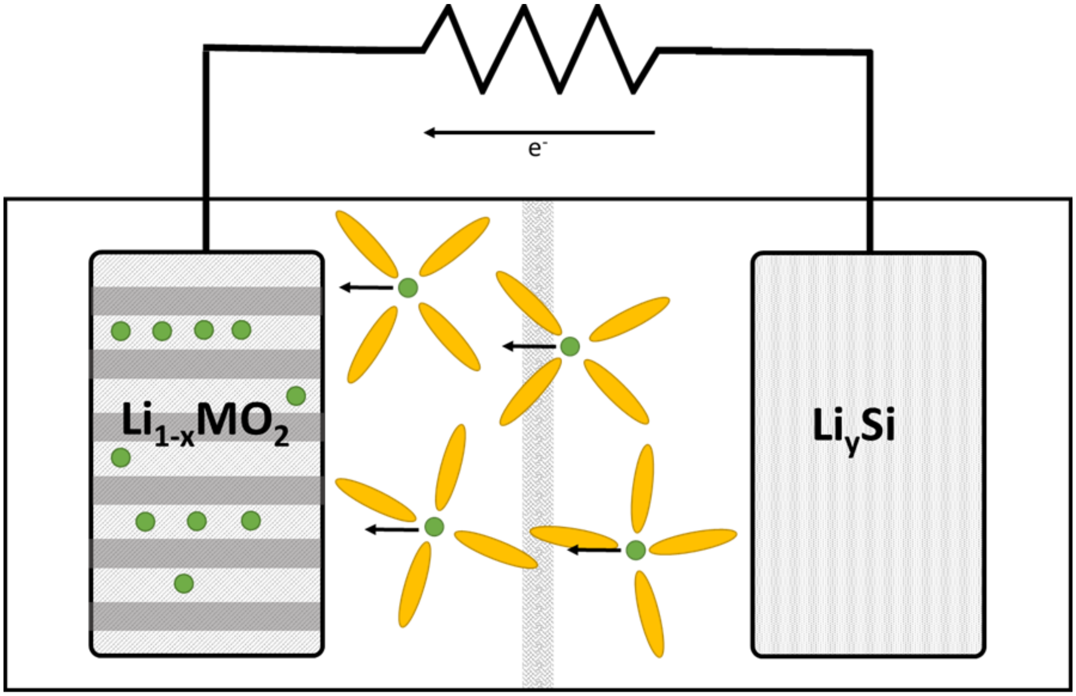

$$Cathode: \quad LiMO_2 \xrightleftharpoons[\text{Discharge}]{\text{Charge}} Li_{1-x}MO_2 + xLi^+ + xe^-$$

$$Anode: \quad Si + yLi^+ + ye^- \xrightleftharpoons[\text{Discharge}]{\text{Charge}} Li_ySi$$

$$Full\ Cell: \quad LiMO_2 + \frac{x}{y}Si \xrightleftharpoons[\text{Discharge}]{\text{Charge}} \frac{x}{y}Li_ySi + Li_{1-x}MO_2$$

Figure 1-1 – A simple lithium-ion battery schematic showing lithium-ion transportation and intercalation into a layered cathode material during discharge and the corresponding electrode reactions

1.2.1 Anode

The two types of anode materials used in cells today are lithium intercalation material and lithium alloying material. Lithium metal anodes once abandoned in 1980's due to safety concerns are attracting more attention in research settings but are not near commercialization.[1,2] The anode in this case is primarily made of high-quality lithium reactive material, blended with conducting carbon to increase electrical conductivity, all held together by a suitable binder. These materials are mixed into a single slurry and spread onto a copper foil current collector. A similar composition will be present for any active material chosen for use in the anode.

The most common type of anode active material is graphite which is an example of a layered intercalation material. A graphite negative electrode will reversibly store these lithium ions between the individual graphene sheets to form LiC_6.[3–5] This is what defines this material as an intercalation material, as the carbon atoms do not form physical bonds with the lithium ions. Carbon based electrodes are a very attractive material offering low average operating potential, very little volume expansion during lithiation and the ability to cycle reversibly for thousands of cycles.[4,6,7] This type of reversible intercalation mechanism is also seen in other carbon materials such as petroleum coke.[8,9] Different types of hard or soft carbons offer varying specific capacities and will depend on the heat treatment temperature used in the synthesis.[3,9] Alternative non-carbonaceous intercalation anode materials are commercially available such as lithium titanium oxide (LTO). LTO offers enhanced safety, high operating voltage but has a modest specific capacity of only 175 mAh/g compared to 372 mAh/g for graphite.[10,11] Due to this capacity limitation LTO is not widely used commercially.

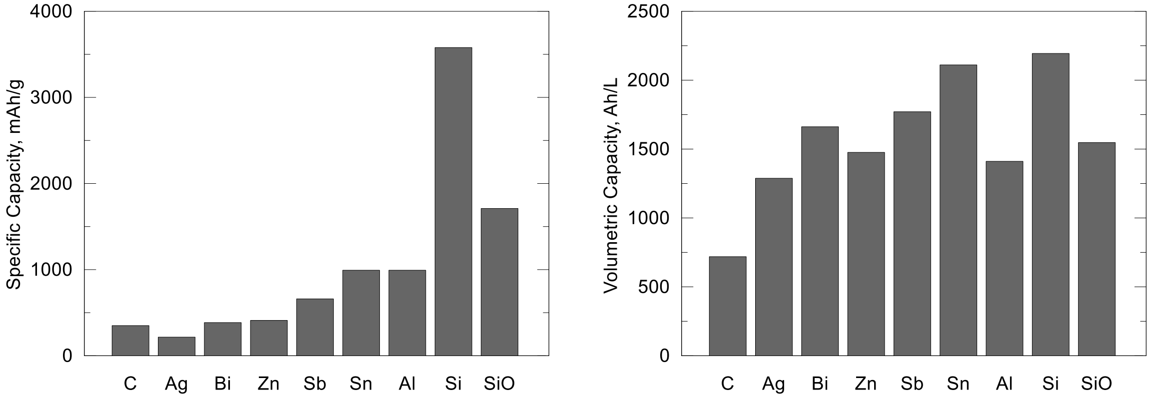

Figure 1-2– Specific and volumetric capacities of anode material based on data presented by Obrovac and Chevrier [7]

The introduction of lithium alloying electrodes is motivated by their potential to offer much larger specific and volumetric capacities compared to intercalation electrodes such as graphite. This is illustrated in Figure 1.2. These materials can offer as much as ten times the specific capacity and three times the volumetric capacity of a graphite anode, but do not yet have the same cyclability and lifetime.[7,12] Alloy electrodes have impressive theoretical capacities but are plagued by capacity loss during cell cycling. This electrode capacity loss is in part explained by the large volume expansions and contractions of the alloy materials during lithiation and delithiation causing particle dislocation and lithium consumption.[7,13–15] The volume expansions of common anode materials are given in Figure 1.5. Research around alloy electrodes has been focused on tin and silicon active materials as they offer the most benefit for a switch away from graphite. At this time work done on tin-containing electrodes has been largely abandoned commercially.

1.2.2 Solid Electrolyte Interphase – SEI

The solid electrolyte interphase is a passive inactive barrier formed between the anode material particles and the electrolyte.[16–18] During the first electrochemical reaction of an electrode, active lithium reacts with electrolyte products at the anode to form this ion-passivating, electron-insulating layer.[16,18,19] This layer has been shown to contain many insoluble products formed in the reaction between active Li and the electrolyte solution and behaves like a solid electrolyte.[16] The proposed model of this SEI formation, shown in Figure 1.3, follows a mosaic model of the SEI consisting of many different materials including LiF, Li_2CO_3, $LiCO_2$-R, Li_2O, lithium alkoxides, and nonconducting polymers.[20] Formation of the solid electrolyte interphase is described as similar to the natural oxide layer formed on the surface a metal, when exposed to air, that helps slow further destructive reactions.[21] The formation of the SEI prevents extreme cell deterioration by preventing or slowing reactions between intercalated Li and electrolyte.[17,18,22] The formation of the SEI is a fundamental reaction, critical to reversible cycling performance, and can be easily tuned and modified through electrolyte additives.[18,19,23] The repeated cracking and repair of the SEI consumes active lithium and results in continuous capacity loss.[17,22] Monitoring the SEI layer, it has been shown that the repeated growth of the SEI upon charge and discharge can be directly correlated to the aging effects of a battery.[17,24] The growth of the SEI on carbonaceous anode material has been correlated to a performance decline proportional to $t^{-1/2}$.[17,24] This finding shows that the SEI is continually growing with time and not only related to cycling effects.

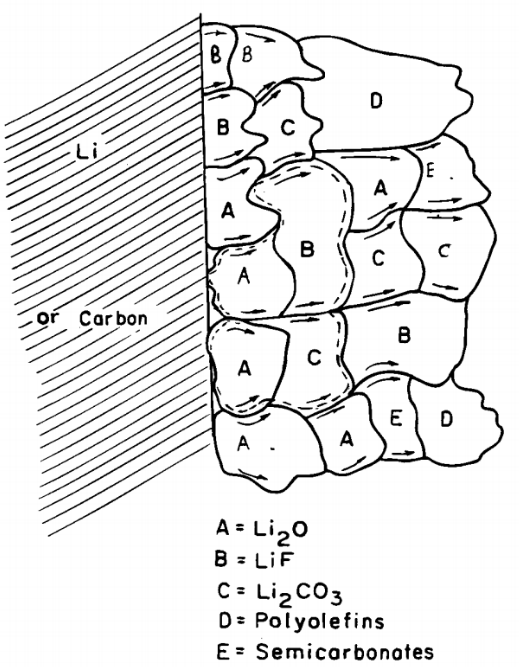

Figure 1-3 - SEI model proposed by Peled [20] highlighting the mosaic model of solid electrolyte interphase (SEI) formation

1.3 SI AND SIO ANODE DEVELOPMENT

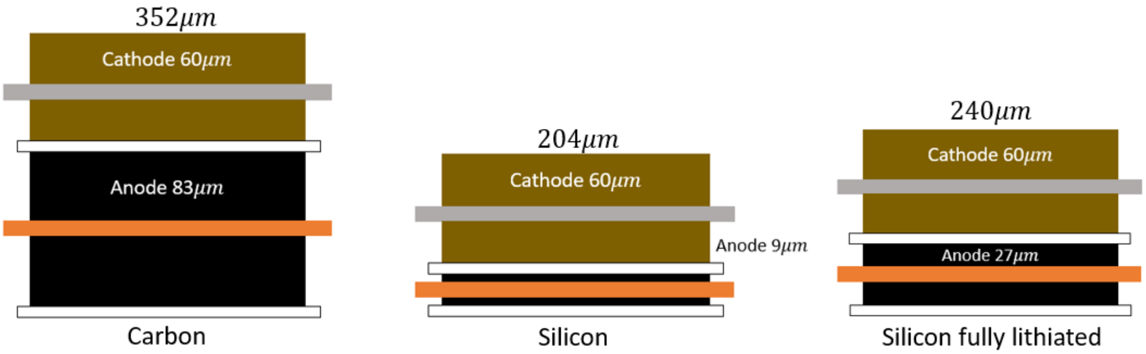

Figure 1-4 – Electrode stack thickness comparison showing the advantages of using a silicon alloying electrode vs. a common graphite intercalation anode

As shown in Figure 1.2, the various alloying type electrodes offer significant advantages in term of specific capacity and volumetric capacity versus intercalation materials.[7] Of the materials listed, only silicon is undergoing serious efforts to be turned into a viable electrode material. The introduction of silicon as an anode material is motivated by its large advantages in specific capacity versus the popular graphite anode. A fully lithiated silicon electrode has a theoretical specific capacity of 3579 mAh/g versus 372 mAh/g for a graphite electrode.[3,25] Comparing these materials in terms of the electrode stack thickness reveals the scale of this capacity advantage. Pairing graphite with a standard NMC cathode 60 µm thick means we need to have an anode thickness of 83 µm. Pairing this same cathode with a silicon electrode, only a 9 µm thick anode is needed. This is a stack energy density increase of 72% (Reduced to 47% when taking into account the volume expansion of lithiated silicon). The large specific capacity comes at the cost of huge volume expansions of 280%, which will lead to rapid cell failure due to repeated cracking of the SEI.[7,13–15] By comparison, a fully lithiated graphite anode will only expand 10%, giving much more favorable conditions for long cell lifetime.[7] This fact is further explained by the data presented in Figure 1.5 which shows the volume expansions of common alloy materials in comparison to graphite.[7] With such large volume expansions it is easy to see how these mechanical stresses are an important failure mechanism.

Due to the reduced lifetime of silicon anodes, a composite mixture of silicon and graphite is normally used. Silicon is often blended with graphite to boost specific capacity of the anode while retaining the excellent cycle life of graphite anode materials.[26–29] This is due to the way lithium will intercalate/alloy with the composite electrode. During lithiation the silicon and graphite portions of the electrode will lithiate almost simultaneously, provided they were both fully delithiated.[30,31] Due to the voltage hysteresis behavior of silicon, the lower voltage graphite portion will be delithiated first below ~0.23

V while the silicon portion remains lithiated.[30,31] This mechanism means the lifetime of a silicon-graphite composite electrode can remain similar to that of pure graphite during shallow charge and discharge cycling. This type of cycling is particularly useful in electric vehicles where full battery discharging is rare. When used for full charge and discharge cycling the vast volume expansion of silicon in the composite will cause loss of electrical contact between active particles and SEI growth.[28,32]

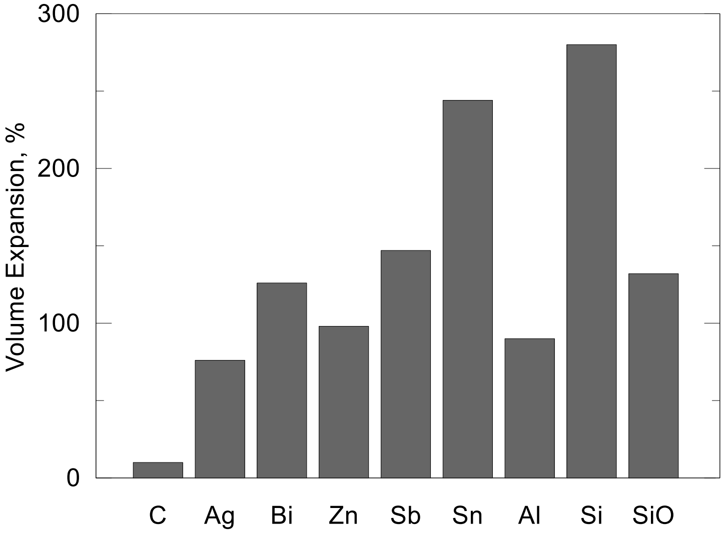

Figure 1-5 – Electrode volume expansion during full lithiation based on data presented by Obrovac and Chevrier [7]

In place of pure silicon, an SiO-graphite blend is commonly used.[33] The use of silicon monoxide (SiO) in place of silicon in negative electrodes is driven by the increased stability on SiO compared to just silicon. SiO is a combination of Si and SiO_2 made to create a volume expansion buffer and provide a less SEI-damaging lithiation process. Battery grade SiO is not simply a blend of Si and SiO_2. Models of SiO creation describe the material as nanoscale regions of Si and SiO_2 surrounded and connected by a matrix of silicon suboxide, (SiO_x where $x < 1$).[34] This model as described by Hohl et al, can be shown visually as in Figure 1.6. This theory is further confirmed by the XRD scans of each material that offer insight into the structure of SiO seen in Figure 1.7. The peak broadening seen in the SiO XRD scan confirms the nanoscale regions of crystalline silicon, and the broad oxide feature that appears around 23°. It has been shown that the supporting matrix of silicon dioxide and silicon suboxide act as a volume expansion buffer limiting volume expansion to only 132%.[7] During the first lithiation of an SiO anode, lithium will irreversibly react with the SiO_2 and SiO_x to form lithium silicates and lithium oxides that provide a volume expansion buffer that will enhance cycle stability.[35,36] These solid volume expansion buffers paired with a highly elastic polymer binder will reduce SEI fracturing and active lithium consumption to give a longer cell lifetime.[35–38] The negative side to this automatic electrode stabilization is the low first cycle coulombic efficiency (CE). With the formation of inactive lithium silicates and lithium oxides, the first cycle coulombic efficiency of SiO drops to ~77%.[35,39,40] This low first cycle CE will not be eliminated but will be reduced using SiO_x, with $x < 1$, in place of SiO. Tuning this oxygen content to improve first cycle CE and still provide a large stabilizing matrix for cycling must be optimized.[41,42]

Currently SiO is made by simultaneous evaporation of stoichiometric amounts of Si and SiO_2 at high temperature and in high vacuum.[43,44] Once evaporated, these materials combine to create a gaseous SiO that is then cooled and deposited onto a single substrate and collected as SiO.[43,44] This is a difficult process to scale up to industrial levels. Precise control of the temperature and vacuum is needed to create the proper resultant material as 5 different variants exist based on atmosphere and cooling rates.[43,45] Similar to conventional chemical vapor deposition, plasma enhanced chemical vapor deposition (PECVD) can be used to effectively synthesize SiO using starting compounds such as, SiH_4 and N_2O, or SiH_4 and O_2.[46,47] This is a suitable method when deposition substrate temperatures must stay reasonably low.[47]

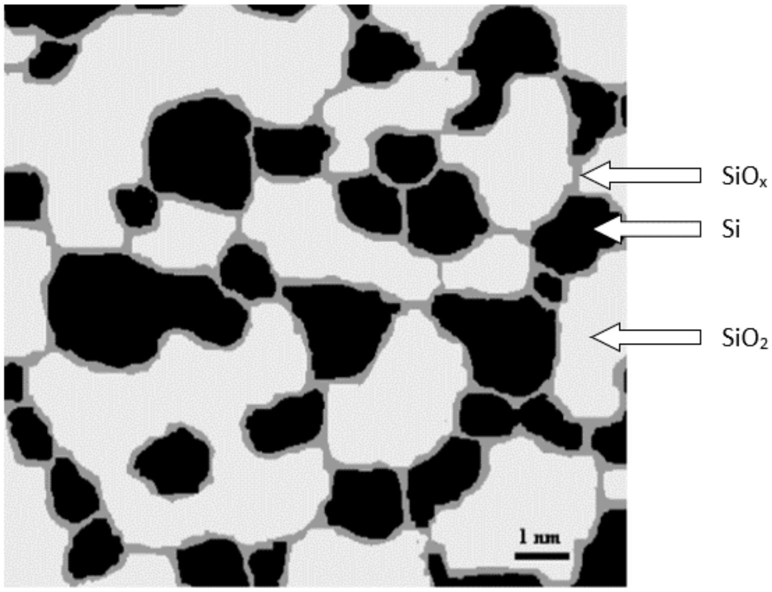

Figure 1-6 – Interface cluster mixture model as proposed by Hohl et al. for the composition of vapor deposited SiO [34]

Recently Cao et al. discovered that SiO_x suitable for use in batteries could be made by ball milling silicon in an oxidizing atmosphere such as air.[42] This process was discovered after a supposedly air sealed ball mill allowed ambient air to enter the milling chamber. Milling silicon powder in the presence of oxygen was shown to induce oxidation of the silicon particle surfaces.[42] Cao et al. showed the production of SiO_x using two methods. Method one ball milled measured amounts of Si and SiO_2 to reach a desired SiO_x compound in the range of $0 \leq x \leq 2$. This method resulted in high iron contamination due to the abrasiveness of the SiO_2 precursor.[42] Method two ball milled silicon in the presence of air to induce the oxidation of silicon. Total milling times were used to control the oxygen content with a maximum oxygen content shown to be x = 0.37 with this method.[42] In this thesis further work is done examining method two, specifically in using a more controlled oxygen delivery system and increased production volume. These areas of research will work towards making the production of SiO_x by ball milling a more industry appropriate method.

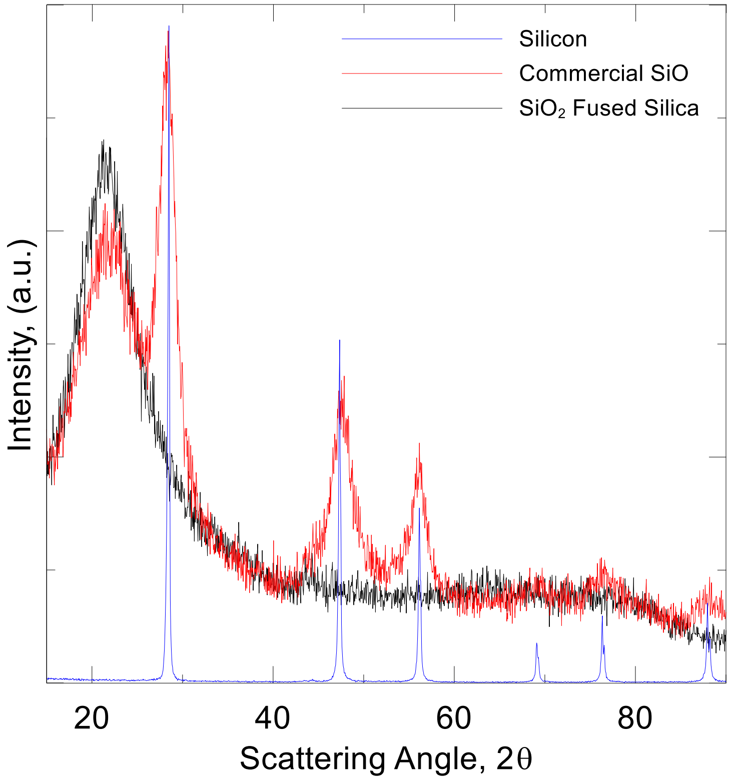

Figure 1-7 – XRD scans detailing the composition of battery grade SiO. Commercial SiO spectrum shows characteristic peaks of both crystalline Si and amorphous SiO_2

CHAPTER 2 MATERIAL PREPARATION

2.1 BALL MILLING

Milling is a mechanical technique that was and is still mainly used for reduction of particle sizes. For many years it has also served as an alternative to more sophisticated methods to combine elements in the solid state down to the atomic level.[48] Mechanical milling and grinding is also known as 'mechanical alloying' and is an effective method of advanced material synthesis, resulting in homogeneous composite particles with uniform internal structure.[49] Mechanical alloying is a dry and high energy milling process that can be used to create composite materials of anything from metallic to ionic elements.[48] Ball milling is not only used to create homogenous alloys of any material, it is also used to accelerate conditions for chemical reactions or induce chemical reactions directly.[50–52]

Mechanical alloying is used to create alloys of materials with widely different melting points, quasicrystal materials and amorphous structured materials.[53] In the milling process energy is imparted to particles in collisions that trap particles between colliding ball bearings or between ball bearings and milling vial walls. In the case of a vibratory mill, particles are subjected to high stresses on the order of 200 MPa for times on the order of microseconds.[48] During these collisions the particles experience severe plastic deformation that exceeds their mechanical strength causing particle fracturing. Shown in Figure 2.1a, these particles experience fracturing and rewelding to another particle in similar particle trapping collisions[48].This process is continually repeated during the course of a milling run until a homogeneous solid-state mixture is reached as shown in Figure 2.1c. During this process there is a balance between particle fracturing and particle binding that results in a stable average particle size in the final mixed material.[48] This balance between fracturing and welding is directly related to milling parameters such as charge to media ratios, ball size, milling duration, and even milling temperature. Kinematic analysis of these ball mills can be used to describe dynamic phase diagrams for specific mixtures under specific milling conditions.[54,55]

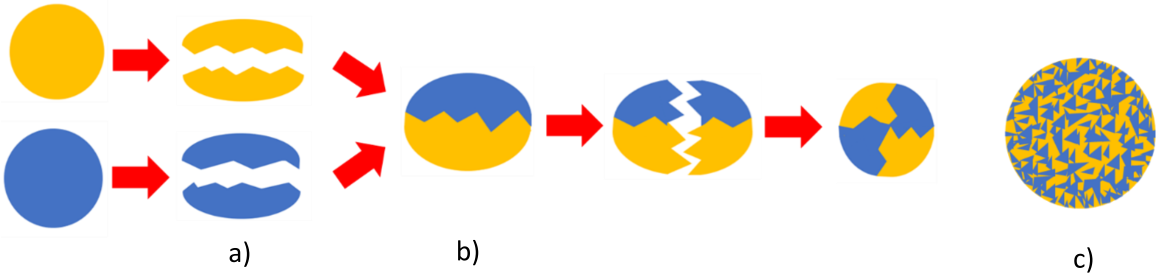

Figure 2-1 – Mechanical alloying process as presented by Gaffet et al.[48] showing a) particle fracturing during collisions, b) particle rewelding, and c) final homogenous composition

Using mechanical milling to speed up or induce chemical reactions is known as mechanical activation or mechanochemistry.[50–52] In the same way mechanical milling can be used to create a homogeneous mixture of two elements/materials, the same milling techniques can be used to develop and distribute a surface oxide evenly throughout a material or composite material.[42,49] For the work described in this thesis, mechanical milling and grinding are used to transform crystalline silicon powder to an amorphous structure before an oxidizing agent is introduced to produce silicon oxide. Following the steps outlined above and visualized in Figure 2.1, the silicon and silicon oxide can form a stable and homogeneous mixture with a controllable ratio of active to inactive material. As explained in the introduction, this can be a suitable replacement method for production of SiO_x synthesized by vapor deposition. There are many different powder milling methods, such as vibratory milling, planetary milling, roller milling and attritor milling. They all achieve broadly the same results, but each technique has their own advantages and disadvantages.

2.2 SHAKER MILL – SPEX 8000

A SPEX 8000D shaker mill (Metuchen, NJ) is a small scale, closed environment, high energy ball mill that is used primarily for pulverization of rocks, minerals, and other hard and brittle material, but is also used for mechanical alloying, slurry grinding, and powder blending.[42,48,56,57] This mill is capable of processing up to 2 g of material at a time with a recommended ball to powder mass ratio of 10:1 for best results. A vibratory mill's small size but high energy milling potential make it a popular choice for lab-scale experiments. The motion of the milling vial, illustrated in Figure 2.2, resembles a figure-8 motion consisting of quick back and forth shakes with short lateral movements. Due to the complexity of the motion, no permanent gas inlet or outlets can be attached to the milling vials. This makes milling under measured gas flow nearly impossible. This combined with the low processing volume per milling vial make the shaker mill less desirable compared to other available milling techniques.

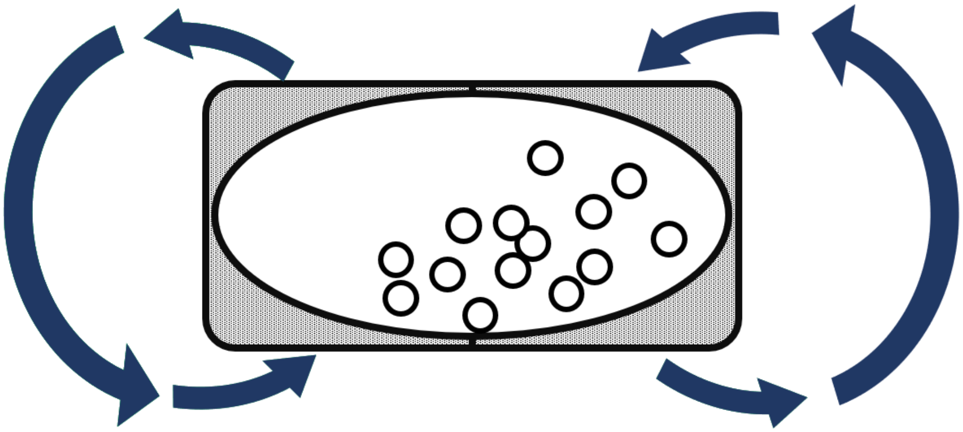

Figure 2-2 – Cross sectional sketch of a vibratory milling vial showing its figure-8 like milling motion

It is important to note that work done by Cao et al. on creating SiO_x powder by reactive milling was completed using a SPEX 8000 mill modified for milling in air or argon atmosphere.[42] The milling vial was prepared and sealed with a removable O-ring under argon atmosphere when air milling was not needed. When needing to introduce oxygen to the sample the O-ring was removed revealing a small, drilled hole through which oxygen could enter the milling vial. This is not seen as a controllable way to introduce the oxidizing agent and other milling techniques were pursued instead.

2.3 PLANETARY MILL

A planetary mill, as depicted in Figure 2.3, consists of two counter-rotating shafts operating at several hundred RPM. Movement of the milling vial is governed by a rotation speed ω and the movement of the large diameter shaft connecting the counterbalance with the sample vial is described by revolution speed Ω. Modern configurations of planetary mills have the rotation axis angled towards the revolution axis for even distribution of forces inside the milling vial.[58] This milling method is similar to horizontal roller milling due to the direction of forces inside the milling vial but has more variety for speeds and energy with the ability to independently adjust the angular velocities of ω and Ω. With this adjustability and at larger scale, a planetary mill can be used for mechanical alloying but in lab scales is primarily used for powder blending and slurry mixing. Similar to vibratory milling, this milling type does not allow permanent gas fittings to be attached in any way.

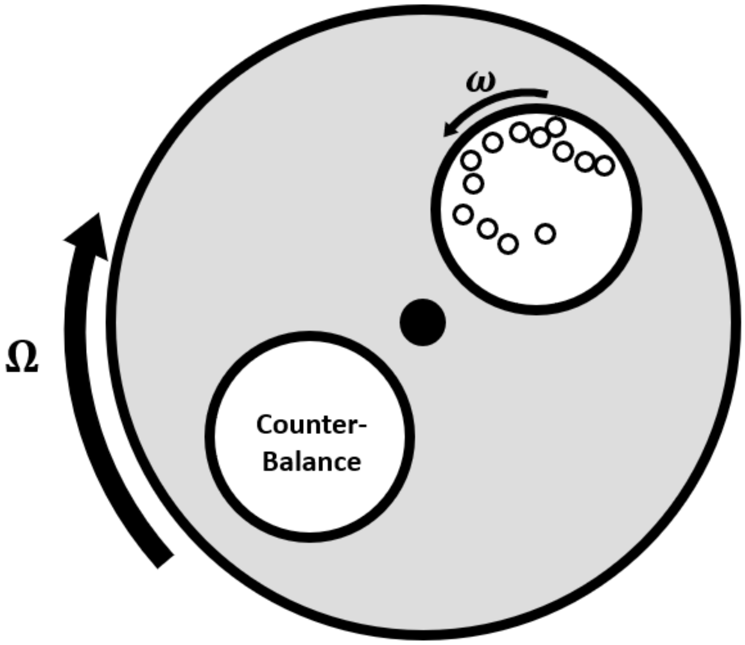

Figure 2-3 – Simple diagram illustrating the motion of a planetary mill

In this work, the two methods selected are roller milling and attritor milling. Each milling technique uses a carefully selected ball milling media based on the mill size and desired particle size. The milling media used in the ball mill and attritor mill are 3/16” 440 hardened stainless steel ball bearings. This small size was chosen to increase the number of powder/media collisions during the milling time with the result of a reduced particle size.

2.4 HORIZONTAL ROLLER MILLING

Horizontal roller milling, or simply known as roller milling, is a very common milling technique used in industry. This method is also correctly known as ball milling, jar milling or pebble milling. Roller milling uses the constant rotational speed of the milling vial to create a grinding and cascading effect of milling media to achieve mixing and mechanical alloying. This cascading effect is what causes media-media and media-vial wall collisions. This is visualized in Figure 2.4. Roller milling is a well-known industrial process with industrial roller mills reaching several feet in diameter (pauloabbe.com). There are several advantages of roller milling on an industrial scale. Unlike many applications, roller milling becomes more energy efficient as the size increases due to the relatively low rotational speeds but large media sizes. The low rotational speeds result in very little excess heat production which will require little to no external cooling. Ball milling offers repeatable results with a narrow particle distribution window, reducing the need for post milling processing such as classification. By fine tuning parameters of the ball mill such as rotational speed, media size, charge to media ratios and milling duration, results achieved on a lab scale mill are easily achieved with scale up to an industrial sized unit.

A lab scale set of roller milling vials, pre-existing from earlier work done within the Dahn lab, were used to evaluate the production of SiO_x by milling. The roller mill vials pictured in Figure 2.4 measure 16.5 cm inner diameter with a chamber length of 4.1 cm. They consist of two identical halves which can be bolted together and sealed using a rubber O-Ring. These milling vials were modified with a Duff-Norton Series 5000 2-way rotating flow joint allowing gas to flow into and out of the milling vial. This was used to control the atmosphere in which milling was done through continuous gas flow. Reduction of crystallinity was done while milling in an inert argon atmosphere. The mechanochemistry of developing and evenly distributing a silicon oxide was done while milling in an oxygen atmosphere. With the attached flow joints we can precisely control the gas flow rate and oxygenation of the SiO_x powder.

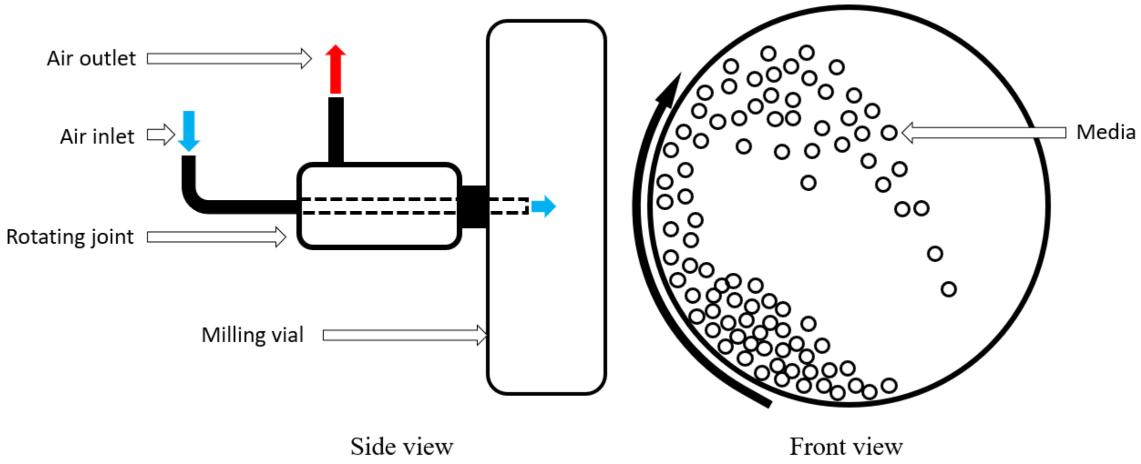

Figure 2-4 – Roller mill cross sectional diagrams showing air inlet, air outlet, and flow joint from the side view, and the cascading media milling effect shown in the front view

Approximately 2500 3/16” (4.76mm) 440 stainless steel ball bearings (BC precision), hardened to 64 HRC, were used as the milling media in our roller mill. This is enough to fill half of the volume of the milling vial and with 50 g of -325 mesh silicon powder from Sigma Aldrich added as the reactant charge gave a milling mass ratio of approximately 40:1. Smaller milling media was chosen to maximize collisions between powder and media while achieving a small particle size advantageous for use as anode material. The correct rotational speed used for the roller mill is related to the diameter of the milling chamber and the 3/16” media. The critical rotation speed of 106 RPM was calculated using Equation 2.1:

$$\nu_c = \frac{30}{\pi}\left(\sqrt{\frac{g}{R-r}}\right) \qquad \text{E2.1}$$

where R is the inner radius of the milling vial, r is the radius of the milling media, g is the acceleration due to gravity, and ν_c is the critical rotational speed of the roller mill in RPM.

For speeds less than the critical rotation speed we will see no cascading effect that leads to the mechanical milling necessary to produce an amorphous SiOx material. This will shift emphasis towards powder grinding and mixing as the media will roll along the bottom edge of the milling vial (Figure 2.5a). Speeds greater that the critical speed will result in milling media pinned to the outer edge of the milling vial as the centripetal force on the media generated by rotation is greater than the downward force of gravity (Figure 2.5c). This was confirmed using a modified milling vial with a transparent window. With this, an optimum rotation speed was found to be slightly higher than the theoretical critical rotational velocity and was set to 116 RPM for a greater cascading effect.

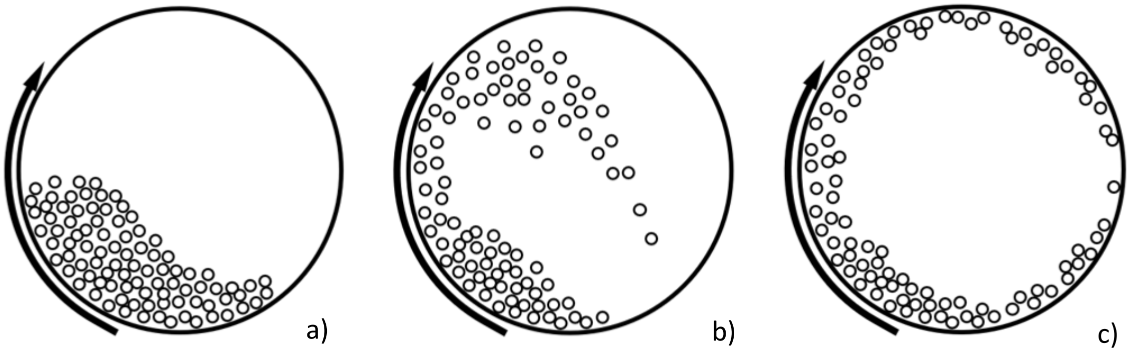

Figure 2-5 – Roller mill rotational speed requirements based on the milling vial radius and media size. a) $\nu \leq \nu_c$, b) ν_c, c) $\nu \geq \nu_c$

Shown in Figure 2.6 is the full roller mill setup used for synthesis. As indicated in the figure we have a gas cylinder and two flow meters allowing full control of the milling atmosphere. The two modified milling vials roll on two rubber coated rollers: one free and one being driven by a 130 V DC motor at a constant speed. The outflow of gas is run through an oil bubbler to ensure there is not backflow of air into the milling vial.

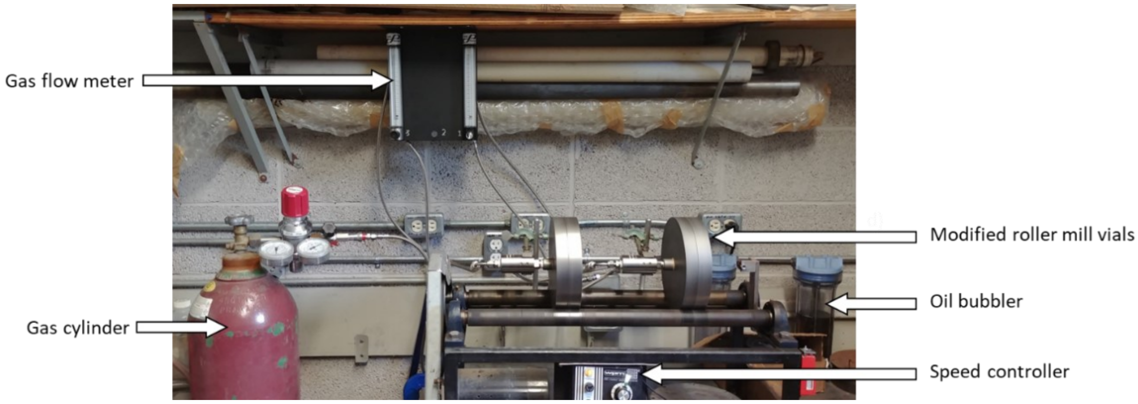

Figure 2-6 – Full roller mill setup labelled and indicated

2.4.1 Roller Mill Modifications

Figure 2.7 below, shows results of roller milling under oxygen flow for a) 250 hours and b) 2 hours at 116 RPM. Looking at Figure 2.7a we can clearly see the formation of a large silicon deposit after a continuous 250 hours that is no longer being milled and mixed. Silicon deposits are also seen beginning to form in panel b of the figure after only 2 hours milling. To combat these silicon deposits a number of potential solutions were tested. Pre-drying silicon powder did not lead to changes in the caking behavior suggesting excess moisture was not the issue. Monitoring the formation of caking deposits through audio signals proved to be inefficient due to the amount of noise produced by the roller mill. External shock of the outside edge of the roller did not lead to any considerable deposit removal and is not a practical long-term solution. Lithium stearate was introduced as an anti-caking agent in small amounts of ~5% by weight which led to softer deposits but did not eliminate formation.

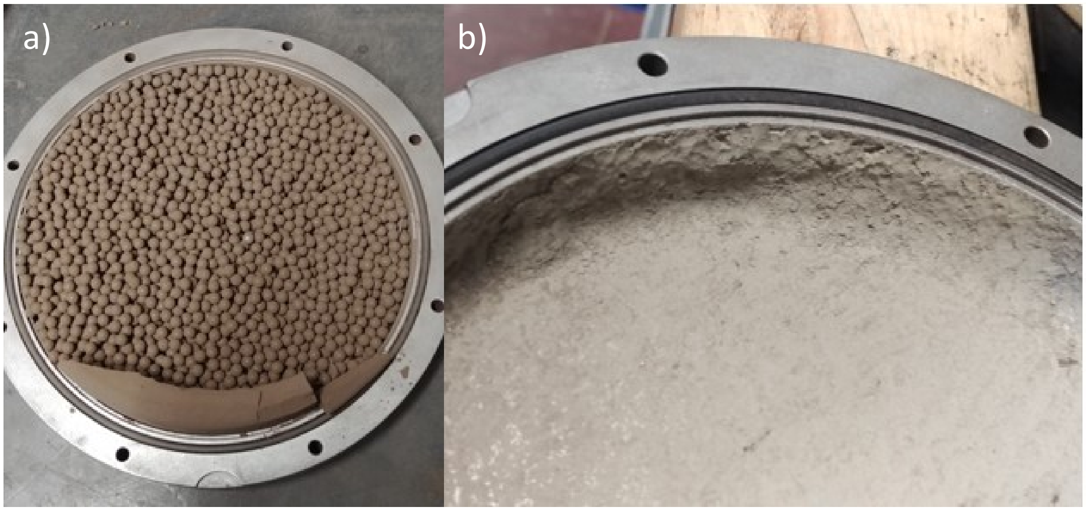

Figure 2-7 – Caking deposits formed during initial roller milling trials after milling for a total of a) 250 hours, b) 2 hours

The final solution to overcome the silicon powder caking came from the attachment of a static scraper blade made to fit inside the milling vial. By extending the input air shaft into the milling vial, a static scraper blade with a fixed length could be attached and used to remove silicon powder from the inside edges of the mill. In this configuration the scraper will remain in an upright position while the milling vial rotates around it. Figure 2.8 shown below details the placement and attachment of the internal scraper. This option proved to be a reliable and low maintenance solution to the problem and was used in all milling trials detailed in this thesis.

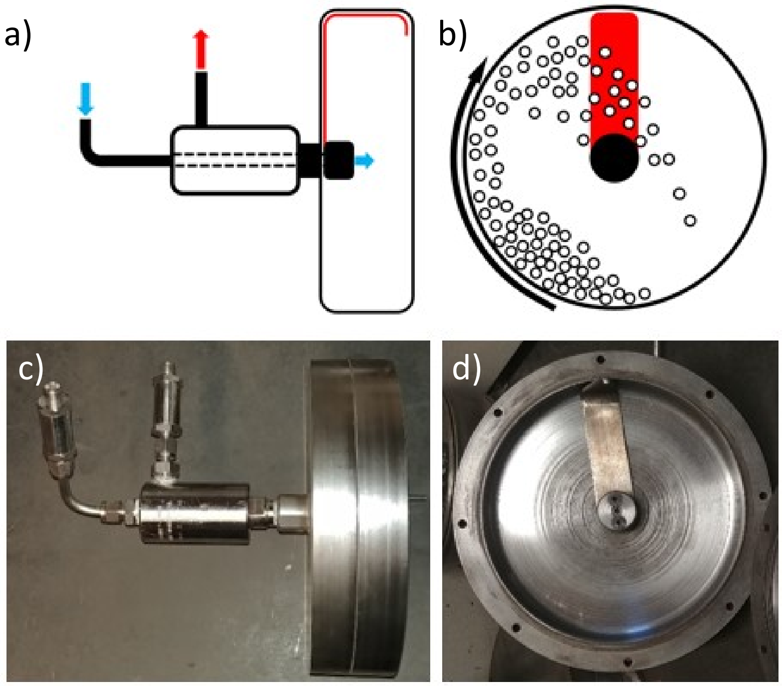

Figure 2-8 – Roller milling vials with attached scraper blade a)/b) Cross sectional schematics, c)/d) Photos of set up

2.5 ATTRITOR MILLING

An attritor mill is different than conventional ball mills discussed above due to its architecture. The methods detailed above involve the external movement of the milling vial imparting energy to the milling media within. An attritor mill is a stirred ball mill which uses a vertically oriented agitator moving at high angular velocity to impart energy to the milling media and is shown in Figure 2.9. With the agitator arms moving at such high speeds, both impact and shear forces are delivered to the material. This chaotic and rapid movement of the milling media results in an efficient grinding and thorough particle dispersion. Compared to conventional ball mills, attritor mills are a more efficient milling process, have a smaller footprint compared to larger, heavier roller mills, and are very versatile with numerous different attachments and accessories available to suit any application. To add to the greater practicality, a stationary milling drum allows easier temperature control using a water jacket and stationary fittings to attach gas lines and control the milling atmosphere.

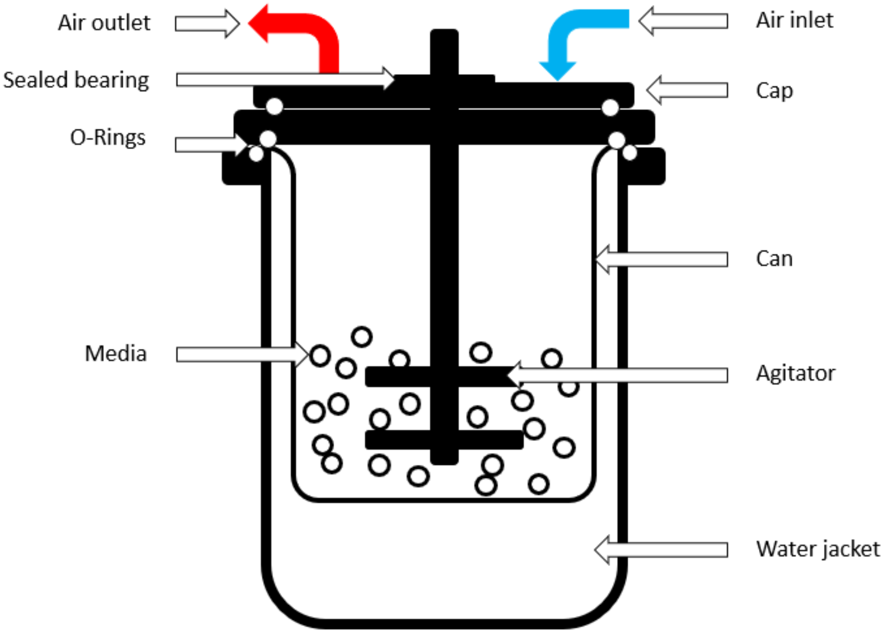

Figure 2-9 – Vertical axis stirred attritor mill. Inlet airflow shown in blue and outlet flow labelled red

Attritor milling can be done as a batch process or continuous particle circulation in both dry and wet milling conditions. Continuous grinding is used to process large quantities of material by continuously feeding powders through at a continuous rate. Continuous processing is recommended in situations where powder caking during milling is a concern. Dry milling in a continuous milling run means the materials will be passed through the milling chamber once at a single feed rate. Under wet milling conditions premixed slurry can be pumped into the bottom of a tall narrow attritor can and discharged at the top. The fineness of the discharged powder will depend on the pumping rate or ‘dwell time’ of the slurry in the attritor can. The addition of a circulation pump and a holding tank means the slurry can be pumped through the milling chambers multiple times, leading to a finer grind. Continuous milling can also be set up for multiple stages. Continuous grinding mills can be set up in series to utilize different sizes of milling media and even introduce new material to add to the mixture. Batch processing is done when the material requires a longer milling time and a controlled milling atmosphere. In this scenario, material is charged into the top of the attritor mill before being milled for the correct amount of time and discharged through the bottom of the tank. Attritor mill sizes can reach capacities of several hundred litres giving excellent variability in the output quantity required.

Figure 2-10 – Full attritor mill setup labeled and indicated as used on the Dalhousie Engineering campus

The attritor mill used here is a lab scale Union Process HD-01 (Union Process, Akron OH unionprocess.com) which is limited to batch processing. This mill uses an agitator rotating about the vertical axis to a maximum of 700 RPM. The custom-made hardened agitator is mounted in the milling cap through a high precision bearing to provide a robust and long-term air-tight seal. As used with the roller mill, we are using 3/16” (4.76 mm) 440 stainless steel ball bearings as our grinding media. For proper milling efficiency a volumetric milling ratio of 225:50 was established for dry milling trials. As shown in Figure 2.9, this mill is equipped with gas inlet and outlets allowing choice of milling atmosphere, as well as water cooling allowing the temperature to be maintained at a constant 20°C. Figure 2.10 shows the full attritor mill setup including the gas bottle and flow meter to create the proper milling atmosphere. Milling is done in a water cooled attritor can sealed with 3 separate O-Rings. Particles carried out of the milling chamber will be captured by a water bubbler attached to the gas outlet. The milling media and 50 g of Si powder are loaded into the attritor can through a small access hole in the cap. Milling was done at a constant rate of 700 RPM to eliminate variability in results.

2.5.1 Attritor Mill Modifications

Dry mill batch processing was completed using the attritor mill. Results when opening the milling chamber showed large, caked silicon deposits similar to that seen during roller mill trials. The initial placement of the agitator height was determined to be too high and silicon deposits formed on the bottom of the attritor can, shown in Figure 2.11a. To combat this problem the agitator was lowered, and the silicon caking began to form on the outside edge of the attritor can; Figure 2.11b. Adjustment of milling ratios and agitator speeds were tried with unsuccessful results. The addition of lithium stearate as an anti-caking agent also did not prove successful. It was then decided that a switch to wet milling was needed to avoid powder caking.

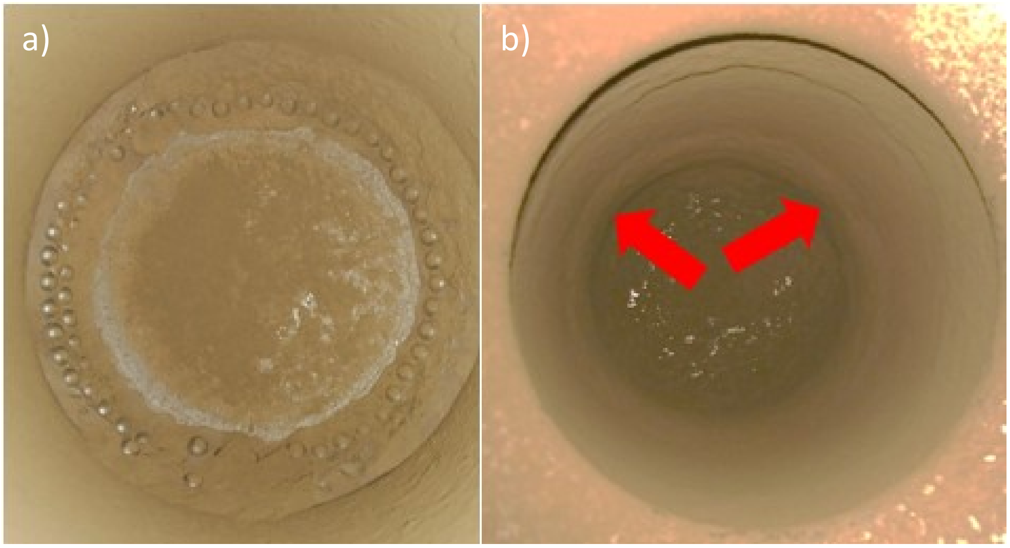

Figure 2-11 – Silicon deposits forming during dry milling trails using the HD-01 attritor Mill. Solid material deposits forming on, a) Lower attritor can corners, b) Attritor can walls

Work done by Kwon et al. showed the ability to oxidize or avoid oxidation of silicon by careful choice of milling solvent.[59] Using these results, anhydrous ethanol was used as the milling solvent while attempting to mill without adding oxygen content.[59,60] Distilled water was used as a milling solvent when wanting to add oxygen content.[59] With the use of distilled water as a milling solvent and an oxidizing medium, we no longer require continuous gas flow for production of SiO_x. The reaction oxidizing the silicon powder will now follow the hydrogen producing reaction given in reaction R2.1. Volumetric milling ratio followed to get a proper slurry thickness for milling was 225:50:100 (Media:Charge:Solvent). This simple transformation was used in all attritor milling trials going forward.

$$Si_{(s)} + 2H_2O_{(l)} \rightarrow SiO_{2\,(s)} + 2H_{2\,(g)} \qquad \text{R2.1}$$

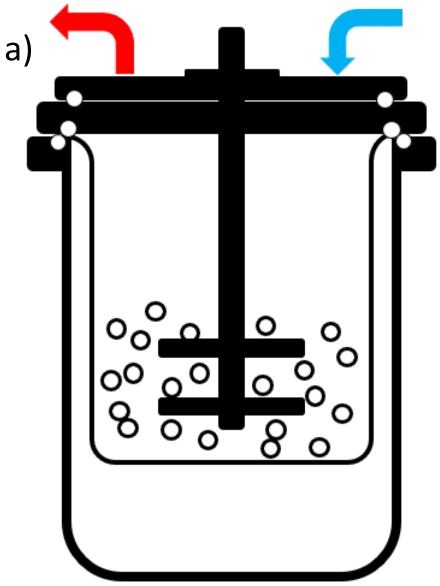

Figure 2-12 – Attritor wet milling transformation. a) Cross sectional diagram during dry milling under gas flow. b) Cross sectional diagram during wet milling in solvent

CHAPTER 3 MATERIAL CHARACTERIZATION

3.1 XRD – JD2000

X-ray Diffraction, XRD, is a non-destructive technique used to identify the crystal structure of a material. In our case it was used to qualitatively identify the degree and rate at which our powder was becoming amorphous. This technique could also be used to qualitatively measure the amount of oxide forming on the powder surfaces.

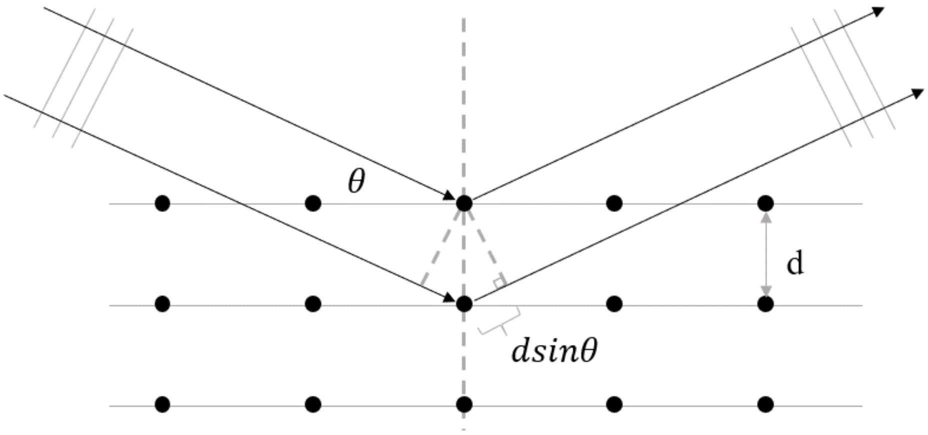

Figure 3-1 – Illustration of Bragg’s law showing reflection of x-rays between parallel atomic planes

X-ray diffractometers consist of three basic parts, an X-ray source, a sample holder, and an X-ray detector. In 1912 it was discovered that crystalline substances act as diffraction gratings when using x-ray wavelengths similar to the plane spacing of the crystal lattice.[61] Utilizing a defined wavelength and specific incident directions, intense peaks of scattered radiation known as Bragg peaks are observed. This interaction of the incident x-rays with the sample produces constructive interference when satisfying Braggs law:

$$n\lambda = 2d\sin\theta \qquad \text{E3.1}$$

where n is the order of reflection, λ is the incident wavelength, d is the material's interplanar spacing, and θ is the incident angle, as depicted in Figure 3.1. Scanning the sample through the range of 2θ angle will reveal all possible diffraction directions due to the random ordering of the powdered material. Using Bragg's law, important information about crystal structure can be determined such as atomic planar spacing and unit cell dimensions.

In a perfect crystalline material, the resultant XRD pattern would appear as a series of delta functions at the angles at the correct Bragg angles. In practice, a real material will have smaller crystalline domains making up the full material. These smaller crystalline regions will be reflected in the resulting XRD patterns and cause peak broadening. Information about the size of crystalline regions in the material can be measured using the Scherrer equation:

$$\mathrm{w} = \frac{0.9\lambda}{\mathrm{t}\cos\theta} \tag{E3.2}$$

where λ is the X-ray wavelength, t is the peak full width at half maximum (FWHM) given in radians, and θ is the Bragg angle of the peak.[62,63] The Scherrer equation uses the FWHM of the diffraction peaks along with the Bragg angle to calculate the size of the crystalline regions. The Scherrer equation is effective for estimating crystalline domains through the range of $2 \leq \mathrm{w} \leq 100$ nm.[64] Domains larger than this will have a peak width at half maximum less than 0.1° and require more precise methods of measurement. Domains smaller than 2 nm will have peak widths greater than 5° and the Scherrer equation must be modified for material strain effects.

XRD data was collected using a JD2000 diffractometer utilizing Cu K_α x-rays and a diffracted beam monochromator. This diffractometer uses Bragg-Brentano geometry meaning the sample and detector are rotated through the programmed incident angles around a stationary x-ray source. This unit is equipped with divergence slits to control the sample irradiation area and receiving slits to control the signal to noise ratio of our results. Standard XRD scans were done from 15-90° with 0.5° step size and a 3 second dwell time. The divergence slits were set for 1° and receiving slits set to 0.2 mm.

3.2 BET SURFACE AREA MEASUREMENT

BET surface area analysis was used to measure the specific surface area of the milled silicon samples removed from the ball mills. This method developed by Stephen Brunauer, Paul Emmett, and Edward Teller is an extension of the Langmuir theory which describes the adsorption of gas molecules onto a solid surface. BET works by quantifying the amount of gas that can be adsorbed onto the surface of a solid. The amount of gas adsorbed will depend largely on the amount of exposed surface but also on parameters such as temperature, gas pressure and the strength of the interaction between the gas and the solid.

Measurement was completed using a Micromeritics Flowsorb II 2300 Surface Area Analyzer (Micromeritics, Norcross, GA) using nitrogen as an adsorption gas and helium as a carrier gas in a 30/70mol% mixture. The analyzer is calibrated by injecting 1.0 mL of nitrogen gas through a septum located after thermal conductivity cell #1, as depicted in Figure 3.2. At 22 °C and atmospheric pressure, 1.0 mL N_2 will give a surface area reading of 2.84 $\mathrm{m^2}$. Glass sample tubes are filled with approximately 1.0 g of material or enough material to reach the recommended 20 $\mathrm{m^2/s}$ adsorption rate.[65] Before analysis, each sample is dried and degassed at 120°C for 45 minutes to remove excess moisture and trapped gasses that would interfere with measurement. A cold trap is used at the gas inlet to reduce impurities in the gas.

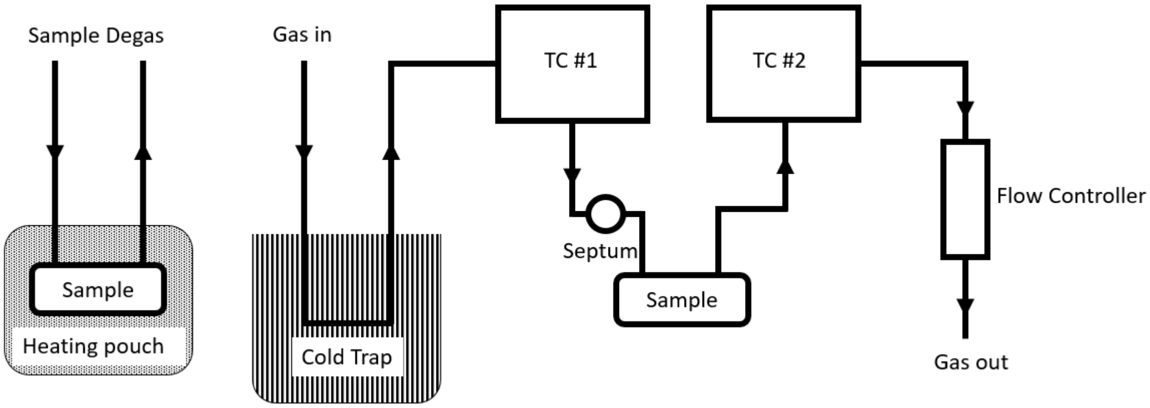

Figure 3-2 – Micromeritics Flowsorb II 2300 gas flow schematic and separate sample degas connections

To quantify the amount of nitrogen adsorbed and desorbed to our solid material, two gas thermal conductivity cells are placed in series before and after the sample holder tube. This is shown in Figure 3.2, labelled TC #1, and TC #2. As a result, this causes the thermal conductivity of the gas in the post sample thermal conductivity cell to increase in reference to cell #1 as nitrogen is adsorbed. The difference in the thermal conductivity in each cell is used quantify the number of adsorbed nitrogen molecules. As the sample is cooled in liquid nitrogen, nitrogen molecules from the mixed gas adsorb to the solid surface and an adsorption rate is displayed by the Flowsorb II. Adsorption is said to be complete when the rate of adsorption returns to below 0.02 m^2/s.[65] The sample holder is then warmed with room temperature water and the Flowsorb II displays desorption rates. The adsorption and desorption areas should be the same in a correct measurement. The average between the adsorption and desorption surface area are divided by the mass of the material to give the specific surface area of the material.

3.3 MOSSBAUER SPECTROSCOPY

Mossbauer spectroscopy was used to determine the amount of iron contamination in our final samples as a result of continuous ball milling. A Mossbauer Spectrometer is a tool used to probe a material at the atomic level and give further insight into its composition. Mossbauer spectrometry operates based on small shifts in nuclear energy levels due to the chemical environment. In a typical gamma ray emission, some energy is transferred to the nucleus to conserve momentum. In this same way during gamma ray absorption the absorbed energy is reduced by the recoil energy. The recoil energy measured is given in Equation 3.3[66]:

$$E_R = \frac{E_\gamma^2}{2Mc^2} \qquad \text{E3.3}$$

where E_γ is the absorbed gamma ray energy, M is the mass of the nucleus, and c is the speed of light. When measuring the gamma ray emission from a gas, the mass of the nucleus is small, resulting in a large recoil energy. This will be detected as a small resonance. When examining solids, the emitting and absorbing nuclei are bound in a lattice, resulting in the recoil of the lattice as a whole. The recoil energy is very small as M is taken to be the mass of the entire lattice. The gamma ray transition energy can then be detected through the lattice vibrations. The finite probability that the energy decay occurs without a phonon is known as the recoil free fraction (RFF).[67] The phenomenon of recoil free nuclear resonance emission or absorption of gamma rays by a nucleus is known as the Mossbauer Effect.[67]

During data collection the material of interest is placed in between the gamma ray source and the detector and receives a source energy of E_γ. Atoms of the same element in the sample will have a transition energy of $E_\gamma + x$ where x describes an energy shift owing to the chemical nature of the local environment. To reach resonant absorption, the energy of the γ-rays must match the energy of the atom $E_\gamma + x$. This energy can be tuned to reach this resonant absorption level through the use of the doppler effect where:

$$E_D = E_\gamma + E_\gamma \frac{v(t)}{c} \qquad \text{E3.4}$$

where $v(t)$ is the source velocity and c represents the speed of light. Using this equation, resonant absorption will occur at $x = E_\gamma\ v(t)/c$. The resulting spectrum collected of γ-ray transmission versus source velocity is known as a Mossbauer spectrum.

Quantitative Mossbauer spectroscopy is a more difficult process to complete as the spectral area presented does not only depend on the number of ^{57}Fe nuclei present but also on the RFF of the sample. This RFF value can be calculated using the two-lattice method. This method uses a single room temperature measurement on a two-foil absorber to measure the relative integrated intensity of two compounds simultaneously.[68,69] When two phases i and j are present in a sample in known amounts, the RFF of the two materials are related by Eq.3.5:

$$f_j = \frac{N\left(^{57}\mathrm{Fe}\right)_i f_i A_j}{N(^{57}\mathrm{Fe})_j A_i} \qquad \text{E3.5}$$

Where f is the recoil free fraction, $N(^{57}\mathrm{Fe})$ is the number of Fe atoms in the sample, and A is the integrated Mossbauer peak intensity.[68] It should be noted that this relationship is accurate within the thin absorber limit. Samples thicker than the thin absorber limit will no longer provide a linear response. Since Mossbauer spectroscopy is sensitive to a host of parameters including impurities and grain size, the RFF value must be determined for each sample being measured. In response to this, a single response factor, F_R, encompassing all effects that will impact RFF determination, is used to relate the integrated intensity of one Fe-containing species to another.[69] Quantitative phase analysis is enabled by adding an internal standard for which F is known. The amount of Fe in a sample can then be expressed in terms of the amount of Fe in the internal standard (IS) by[69]:

$$N(^{57}\mathrm{Fe})_{\mathrm{unk}} = \frac{N(^{57}\mathrm{Fe})_{\mathrm{IS}}}{F_{\mathrm{unk}}} \frac{A_{\mathrm{unk}}}{A_{\mathrm{IS}}} \qquad \text{E3.6}$$

where A_{unk} is the integrated Mossbauer peak intensity for the Fe in the sample with unknown concentration, A_{IS} is the integrated Mossbauer intensity for the Fe in the internal standard, and F_{unk} is the response factor for the Fe in the material with unknown concentration

An Fe_2O_3 internal standard and the sample to be analyzed are homogeneously mixed together with a plasticizer and solidified to form the thin Bellcore film containing a uniform sample mixture. Bellcore plastic films were originally designed for use in Li-Polymer batteries because they offer excellent coating homogeneity.[70] For best results, it is important that the amount of Fe in the internal standard and the sample contain roughly the same amount of Fe nuclei. Trial films are first made to approximate the contamination percentage before a final test sample is created with a closely matched Fe content. Resulting films are analyzed and the data is fitted using Recoil Mossbauer Spectral Analysis software (Department of Physics, University of Ottawa). The total integrated intensity of each identified species was used to quantify iron content using the response factor found for the 10% weight standard Bellcore film.[69] Shown below in Figure 3.3 is a sample data collection taken from work done by Scott et al. showing the distinct increase in the resonance peaks of iron contamination in ball milled silicon samples.[69]

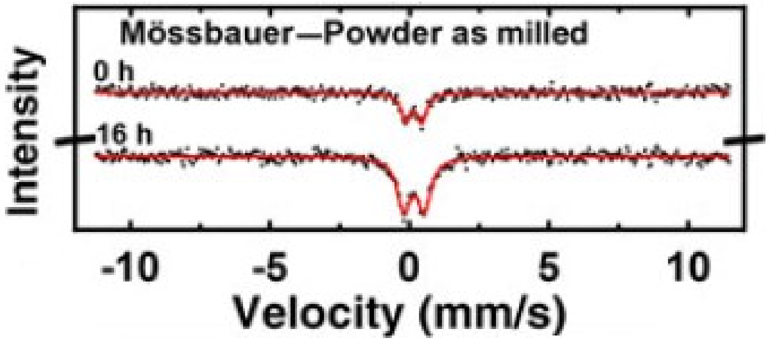

Figure 3-3 – Sample data of ball milled silicon powders as presented by Scott et al [69] showing an increase in $FeSi_2$ peak intensity after milling

3.4 KOH OXYGEN DETERMINATION METHOD

Commonly, oxygen contents of a material are measured through gas fusion analysis (LECO Analysis). [71] To achieve a specific oxygen content in the powder, the oxygen content needs to be measured periodically. Gas fusion analysis heats and vaporizes a sample from a graphite crucible, liberating the oxygen molecules from the powder sample which then react with the graphite crucible to form CO and CO_2.[71] The CO and CO_2, are then swept away with an inert carrier gas and the CO and CO_2 are quantified using an IR adsorption analyzer.[71] This is a specialized test that is time consuming and expensive as samples need to be sent to an external lab. A fast characterization method was needed to determine the oxygen content of silicon, silicon-containing and silicon oxide powder samples synthesized by time-sensitive ball milling.

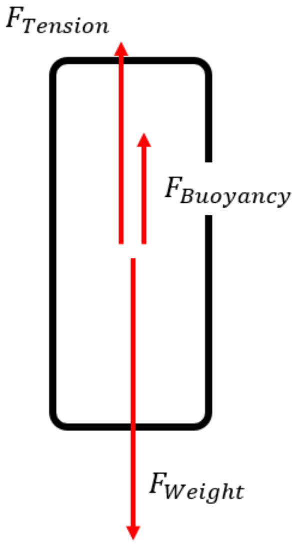

Figure 3-4 - Free body diagram of a pouch bag undergoing Archimedes gas volume measurements

In lieu of an elemental analysis machine or the ability to complete combustion analysis, the method used to determine a powder's oxygen content was based on the reaction between potassium hydroxide, KOH, and the free silicon contained in the sample. This method relies on the quantification of gas evolved in a sealed pouch bag using Archimedes' Principle.[72,73] The change in buoyant force of a sealed pouch bag is being measured as this depends on the amount of gas produced within it. The free body diagram shown in Figure 3.4 can be described by three simple equations shown below as Equations 3.7, 3.8, and 3.9:

$$F_{Bouyancy} = \rho g V \quad \text{E3.7}$$

$$F_{Tension} = m_{scale} g \quad \text{E3.8}$$

$$F_{Weight} = m_{pouch} g \quad \text{E3.9}$$

The buoyant force of an object is given as the density of the fluid, ρ, multiplied by the volume of the fluid displaced by the object, V, and the acceleration due to gravity, g. Equations 3.8 and 3.9 describe the force from the upward tension of the hook holding the pouch bag during weighing and the weight of the pouch bag itself.

Equations 3.10 and 3.11 describe the initial (i) and final (f) measurements of a pouch undergoing gas volume measurements by Archimedes' principle.

$$0 = \Sigma F_{\mathrm{pouch}} = F_{\mathrm{Buoyancy\_i}} + F_{\mathrm{Tension\_i}} + F_{\mathrm{Weight}} \qquad \text{E3.10}$$

$$0 = \Sigma F_{\mathrm{pouch}} = F_{\mathrm{Buoyancy\_f}} + F_{\mathrm{Tension\_f}} + F_{\mathrm{Weight}} \qquad \text{E3.11}$$

Combining these equations using the fact that the weight of the pouch bag and its contents remain unchanged, we arrive at Equation 3.13 describing the volume of gas evolved in the pouch bag as the change in measured mass divided by the density of the fluid.

$$\Delta F_{\mathrm{Tension}} = -\Delta F_{\mathrm{Buoyancy}} \qquad \text{E3.12}$$

$$\Delta V = \left(m_{\mathrm{Scale_f}} - m_{\mathrm{Scale_i}}\right)/\rho \qquad \text{E3.13}$$

This method relies on the reaction of free silicon particles with a KOH-water solution following one or both reactions given as reactions (R1) and (R2).[74] These reactions show that two moles of hydrogen are produced for every mole of free silicon powder placed in the pouch bag. The process to implement this measurement is a simple four step process illustrated in Figure 3.5.

$$\mathrm{Si} + \mathrm{KOH} + 5\mathrm{H_2O} \rightarrow \mathrm{KH_7SiO_6} + 2\mathrm{H_2} \qquad \text{R3.1}$$

$$\mathrm{Si} + 2\mathrm{KOH} + 2\mathrm{H_2O} \rightarrow \mathrm{K_2H_2SiO_4} + 2\mathrm{H_2} \qquad \text{R3.2}$$

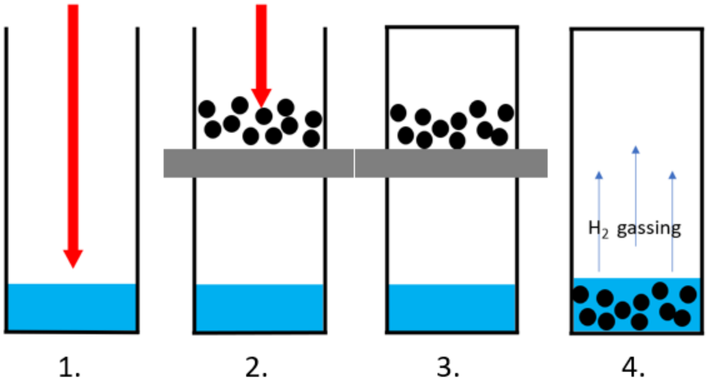

Figure 3-5 – Four step process implementing the KOH oxygen determination method

In step one, a stoichiometrically non-limiting amount of the KOH water solution is inserted into the bottom of the pouch bag using a 1.0 mL syringe. Aluminized pouch bags (CATL, Ningde, China) are used because they are gas impermeable and heat sealable. In step two, the pouch bag is folded and temporarily clamped during preparation at the halfway point to create two separate regions in the single pouch bag. The silicon-based powder to be tested is then placed in the top half of the pouch bag. In the third step, the pouch bag is heat sealed at the top and weighed while submerged to get an initial mass for use in an Archimedes type measurement, also shown in Figure 3.6a. Once an initial mass is recorded, step four is to remove the bag crimp in the middle and allow the two sides to mix completely. The reaction inside the bag will begin to create gas which will be quantifiable with a final submerged mass measurement, shown in Figure 3.6b. The amount of powder placed in the pouch bag should be chosen such that the evolved gas adequately fills the pouch bag without building pressure as this will reduce the volume compared to the volume at 1 atm., and lead to errors in the Archimedes principle gas volume measurement. This is demonstrated with the left-most pouch bag in Figure 3.7. Depending on the surface area and reactivity of the powder, an oxygen content measurement can be made after 5 hours of reaction at 60°C.

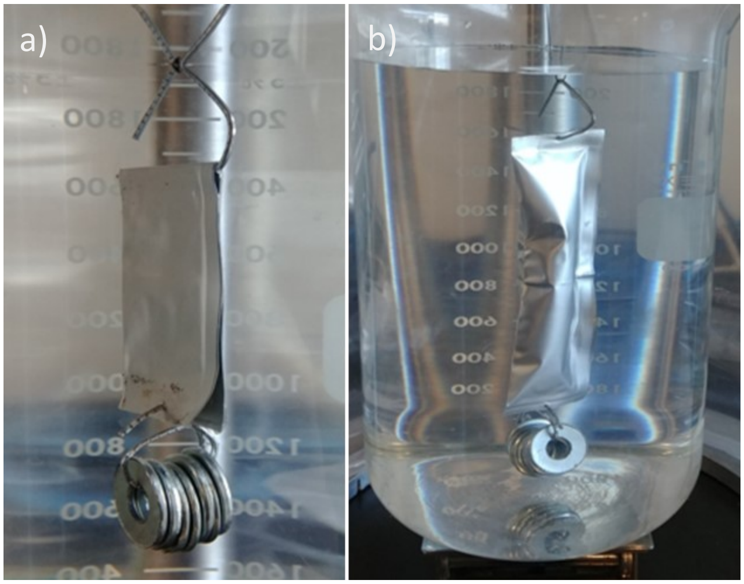

Figure 3-6 – a) Unreacted pouch bag with KOH and SiOx materials separated, b) Reacted pouch bag measuring hydrogen gas evolution

The initial mass of powder placed in the bag is measured to a precision of 0.1 μg using a Sartorius SE 2 ultra high precision balance. The volume of gas produced is measured by the difference between the final and initial mass measurements according to Eq. 3.13. Knowing the initial mass of the powder placed in the pouch bag and the volume of hydrogen produced, hence the moles of hydrogen produced, one can determine a molar ratio of oxygen to silicon. This allows the oxygen content of the unknown powder to be determined.

Verification testing of this method was done using silicon-containing materials of known oxygen content. The results of these tests are shown in Table 3.2. These tests show the accuracy and repeatability of this method.

Table 3-1: Sample data collection for a milled SiO_x sample

Powder	Powder Mass, mg	Unreacted Pouch Mass, g	Reacted Pouch Mass, g	H_2 Gas Volume, mL
Milled SiO_x	7.0935 mg	15.7877	10.0570	5.7307

The density of H_2 at STP and its molecular weight are used to convert the volume of gas to moles. The 5-10 cm depth at which the measurement takes place will result in a small ambient pressure change following $P_a = \rho g h$, and will result in a negligible hydrogen volume change of less than 1%. Following reactions R3.1 and R3.2, where one mole of hydrogen is produced for one mole of reacted silicon, we can calculate that the sample contained 3.58 mg of free Si and by default 3.51 mg of SiO_2. Assuming the sample is simply regions of Si and SiO_2, this 3.51 mg of SiO_2 will contain 1.87 mg O. This sample is then determined to be 26.3% O by mass, resulting in a final composition of SiO_x where x = 0.63.

Table 3-2: KOH method verification testing

Material	**Known Oxygen content** ***O:Si Molar Ratio***	**Measured oxygen content** ***O:Si Molar Ratio***
Silicon #1	0	0.0147
Silicon #2	0	0.0180
SiO_2 #1	2	1.9955
SiO_2 #2	2	1.9929
SiO Vendor A #1	0.904*	1.0354
SiO Vendor A #2	0.904*	1.0242
SiO Vendor B #1	0.888*	1.0199
SiO Vendor B #2	0.888*	1.0308

* LECO Analysis by NSL Analytical

The results from Table 3.2 show inconsistencies with the accuracy of the developed KOH method when testing commercial SiO prepared by evaporation and vapor deposition. This is thought to be the result of Si regions completely encapsulated by SiO_2 within the sample. This would not allow for the reaction of Si particles and KOH solution, resulting in a predicted oxygen content that is larger than the actual composition.

The experimental powder being tested with this method is produced by roller milling silicon powder under oxygen flow. Oxygen content testing of roller milled silicon is completed every 25 hours to monitor the progression the oxidizing reaction. In response to this, a fast, inexpensive oxygen content determination method was needed to reach final oxygen content targets. Figure 3.7 shows five pouch bags all containing KOH solution and ~9.0 mg of Si powder milled under oxygen flow for different amounts of time. Longer milling times mean more SiO_2 production and this is reflected by less hydrogen gas produced in the reaction. The differences in gas production can be seen qualitatively in Figure 3.7, and a quantitative analysis produces the results shown in Figure 3.8. Figure 3.8 shows a smooth curve that can be used to predict oxygen content in SiO_x powder as a function of milling time. The leftmost pouch bag in Figure 3.7 is an example of a pouch bag that contains too much Si powder and the pressure within the pouch has increased past 1 atm. and the result will be disregarded. The tests using fresh silicon powder are completed using less than 7.0 mg to avoid building pressure.

Figure 3-7 – Periodic SiO_x sampling and testing by the KOH method shows less H_2 is produced as more SiO_2 is formed while ball milling

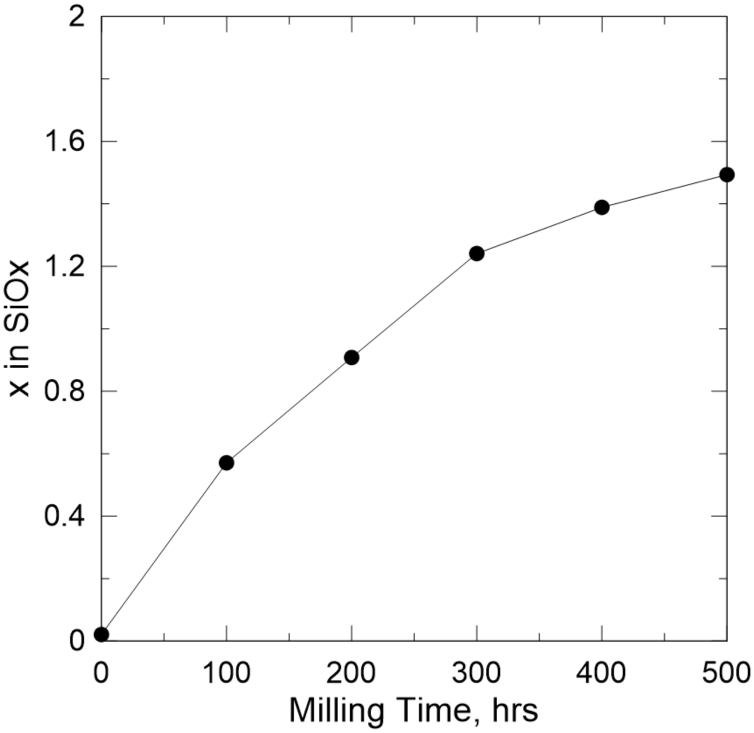

Figure 3-8 – Quantitative oxygen content determination by the KOH pouch bag method showing a steady increase in oxygen content

Figure 3.9 shows a strange effect of pouch bag deterioration after useful results are collected from the pouch bag gassing. The deterioration relates to the exposure of the aluminum pouch material to the KOH solution which is normally separated by a thin polymer layer. This is possibly brought about by imperfections in the polymer layer during manufacturing or caused during execution of this method. Particularly, heat sealing the top of the pouch may be the cause of the deterioration and exposure of aluminum pouch material. As shown in Figure 3.9, there is no expected failure point except the heat-sealed edges of the bag. Reaction between the KOH solution and the aluminum will cause increased gassing and an over-estimate in the amount of free silicon contained in the material. This type of deterioration is not present on every pouch tested but may affect 1 in every 15. As previously mentioned, major deterioration appears long after final measurements of the buoyancy are taken but effects may go unnoticed in the early stages.

Figure 3-9 – KOH pouch bag deterioration due to reaction between pouch bag aluminum and KOH solution

3.5 ELECTROCHEMICAL TESTING

The primary electrochemical testing was done using lithium half cell coin cells. The electrode formula followed an 80/10/10 (SiO_x/CB/Binder) recipe with the addition of 0.1, 0.2, and 0.4 wt% single-walled carbon nanotubes (SWCNT) to improve electrode adhesion and boost conductivity. Electrode dry materials were premixed in a Mazerustar Planetary mixer for one minute to ensure a homogeneous solids mixture. Binders, additives, and solvents were then added to complete the electrode slurry which was mixed for a further two minutes. Binder used is a 25 wt% solution of LiPAA and distilled water (Sigma-Aldrich, US). Conducting carbon is Timcal Super C65 (Imerys Graphite and Carbon, Switzerland). Single wall carbon nanotubes obtained from OCSiAl are a 99.0 wt% distilled water solution containing 0.6 wt% CMC and 0.4 wt% SWCNT (OCSiAl, Luxembourg). The resultant slurry was spread to a thickness of 0.0015" (38 μm) on a sheet of copper foil using a notch bar. The electrode sheets were then dried in air at 110°C for two hours. When dry, 12.7 mm electrode disks were punched from the electrode sheet, giving a final loading of approximately 1.34 mg/cm^2.

Cells were assembled in an argon filled glovebox with prepared electrodes paired with a lithium foil counter electrode as depicted graphically in Figure 3.10. All cells used a standard electrolyte of 1M $LiPF_6$ (BASF, Germany) dissolved in 1:1w EC:DEC (CapChem, China) with 2 wt% VC (BASF, Germany) and 4 wt% FEC (Novolyte Battery Materials Co, China). Five drops of electrolyte were deposited between layers as the coin cells were assembled. Upon completion of the coin cell stack, the cells were sealed using a two-stage pneumatic press to ensure a robust and airtight seal.

Cells were initially lithiated at a current of C/20 before being cycled at a constant current rate of C/10 where cell characteristics such as cycle stability, capacity, and capacity fade could be well monitored. A C/20 check up cycle was done at the end of cycling. Specific capacity vs cycle number, voltage vs capacity plots, and differential capacity plots were the preferred techniques used to evaluate the capacity and stability of the created SiO_x electrodes, with comparisons to commercially available SiO materials. Primary comparisons were done against commercial SiO from vendor A. All cells used for comparisons use the same electrode slurry recipe and preparation process.

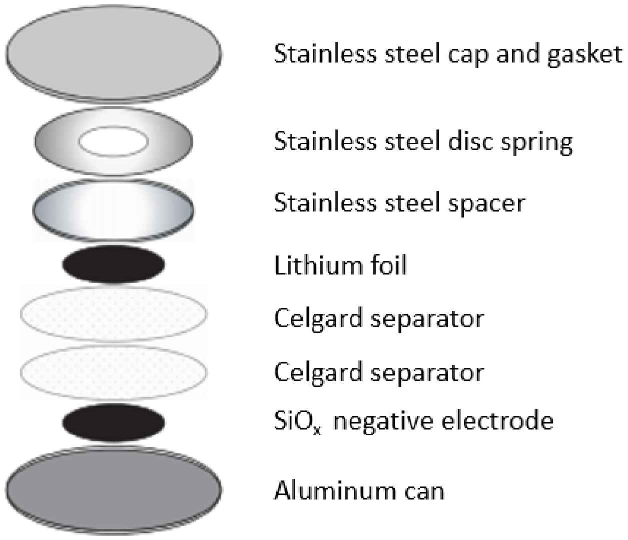

Figure 3-10 - Lithium electrode half cell configuration and assembly order as used in electrochemical testing

3.5.1 dQ/dV Analysis

Differential capacity analysis is a tool that can be used to study the lithiation mechanisms of an electrode material. Differential capacity tracks the electrode's capacity increase on charge or decreases on discharge as a function of voltage. The data presented in these types of graphs can show electrode lithiation stages and phase transformations introduced through lithiation. The example given in Figure 3.11 shows 1.5 cycles of a fresh SiO electrode. During the initial lithiation a large feature is formed at 0.1 V that can be directly connected to the formation of Li_4SiO_4 and Li_2O as active lithium reacts irreversibly with SiO_2 regions. The delithiation peaks present at 0.3 V and 0.5 V represent the low and high voltage delithiation stages of amorphous silicon. The lithiation peaks at 0.1 V and 0.2 V represent the low and high voltage lithiation plateaus of amorphous silicon. The lithiation peak at 50 mV shows the electrochemical conversion of amorphous silicon to crystalline $Li_{15}Si_4$. This analysis can also be used to understand electrode degradation mechanisms brought on through continued cycling.

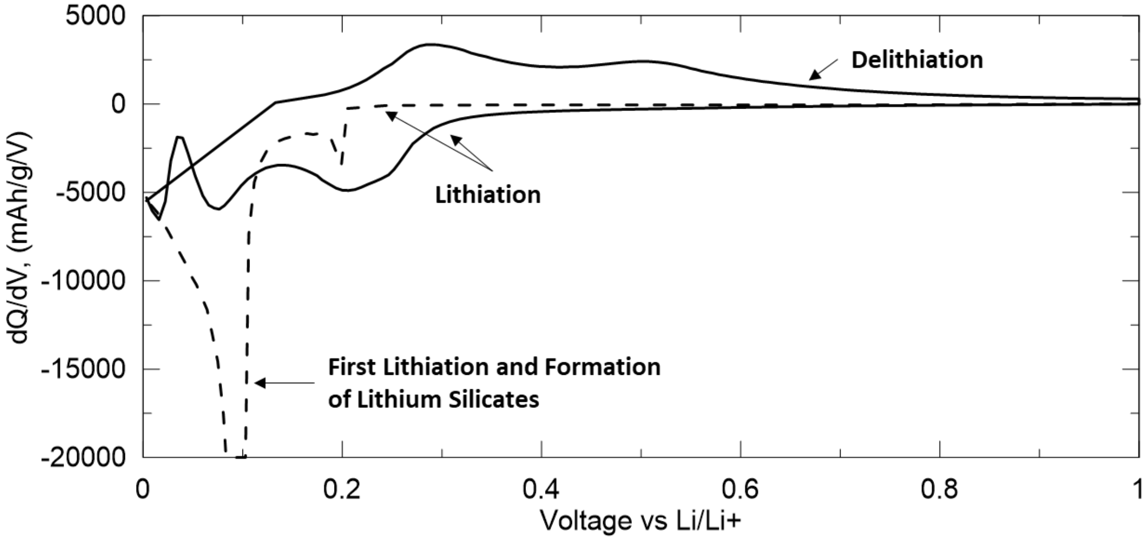

Figure 3-11– dQ/dV sample data for a commercial SiO electrode

3.5.2 V-Q Analysis

This data analysis technique provides insight into the lithiation stages of the electrode based on the cell potential versus lithium metal. Similar to differential capacity analysis, V-Q analysis can be used to identify lithium intercalation/alloying stages present during charge and discharge cycles. The data presented in these graphs can be easily used to monitor irreversible capacity (IRC) losses and cycling behavior. The sample given in Figure 3.12 exhibits an IRC of 26 % and a reversible capacity of 1386 mAh/g. A perfect cell will maintain its capacity and display the same charge and discharge endpoints over its lifetime. When an imperfect cell cycles, the cell discharge endpoint will be different than the previous cycle representing active lithium consumption.

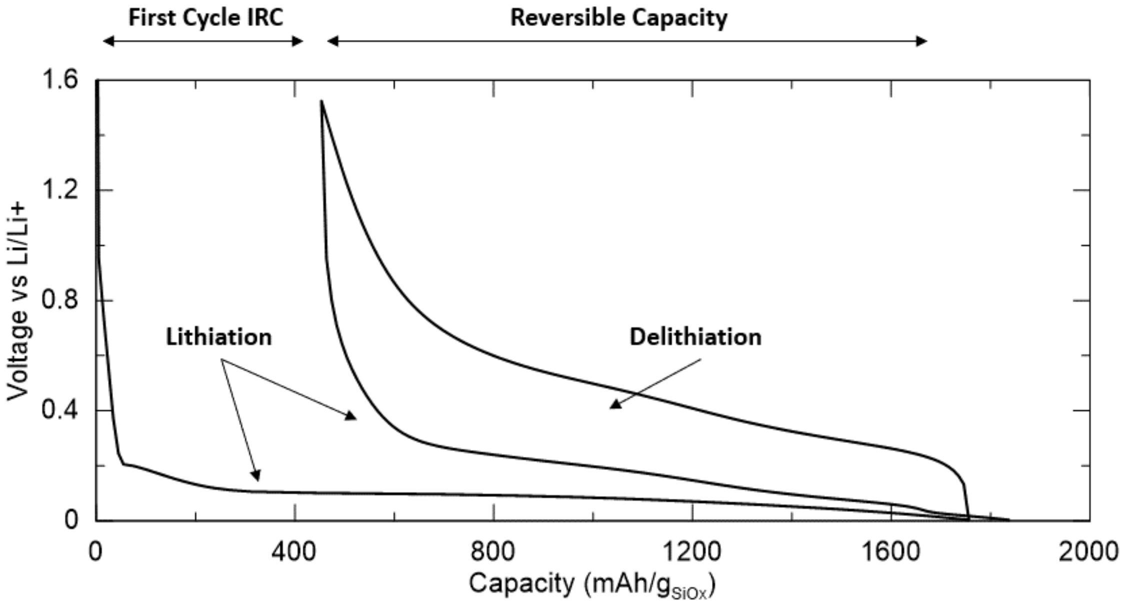

Figure 3-12 – V-Q sample data for a commercial SiO electrode

3.5.3 Cell Cycling

A capacity versus cycle plot gives data that characterizes the lifetime and specific capacity performance of electrodes or full cells. Plots of this type can be used to evaluate cell lifetime or detect failure mechanisms such as electrolyte consumption leading to cell failure.[28] The plot shown in Figure 3.13 is an SiO electrode experiencing capacity roll off around 50-60 cycles.

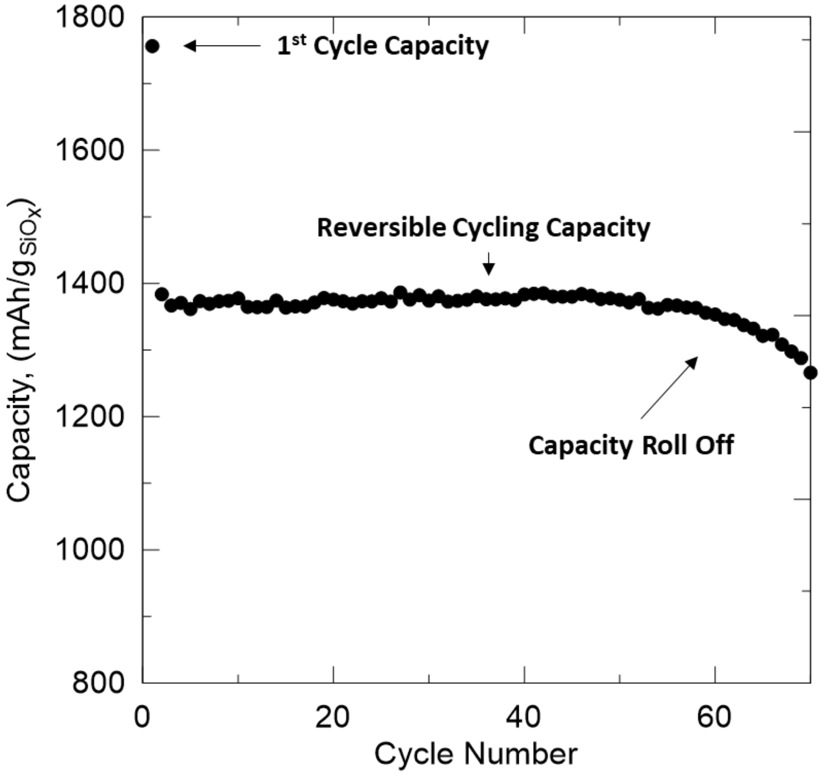

Figure 3-13 – Capacity vs cycle sample data for a commercial SiO electrode

CHAPTER 4 SIO$_X$ CHARACTERIZATION

4.1 LONG RUN DATA COLLECTION

Data was collected on each mill by doing long run milling trials in an oxidizer. From this data we are able to determine important parameters such as total milling time needed to produce an amorphous structure and develop an oxygen content versus milling time relation in the oxidizer used.

Figure 4.1 shows XRD data collected periodically as milling proceeded. Long run milling in the modified roller mill was done under oxygen flow for the entire 500-hour process. Oxygen was passed into the mill at a minimal flow rate of 0.385 L/min to create an oxygen-rich milling atmosphere. Figure 4.1a shows XRD patterns of roller mill samples taken every 100 hours. When taking a sample, the roller mill must be fully stopped, opened, and emptied in order to remove a sample. The roller could then be reloaded with the powder and media to be restarted.

A long run attritor mill trial was done under wet milling conditions with only distilled water used as a milling solvent. Samples from this mill were taken every ten hours for a total run time of 50 hours as shown in Figure 4.1b. Unlike the roller mill, the attritor mill did not have to be fully emptied and reloaded when sampling. The wet milling conditions used in the attritor mill meant that the mixed slurry could be extracted using a wide mouth syringe and resealed. Enough sample was taken to perform XRD and oxygen content analysis.

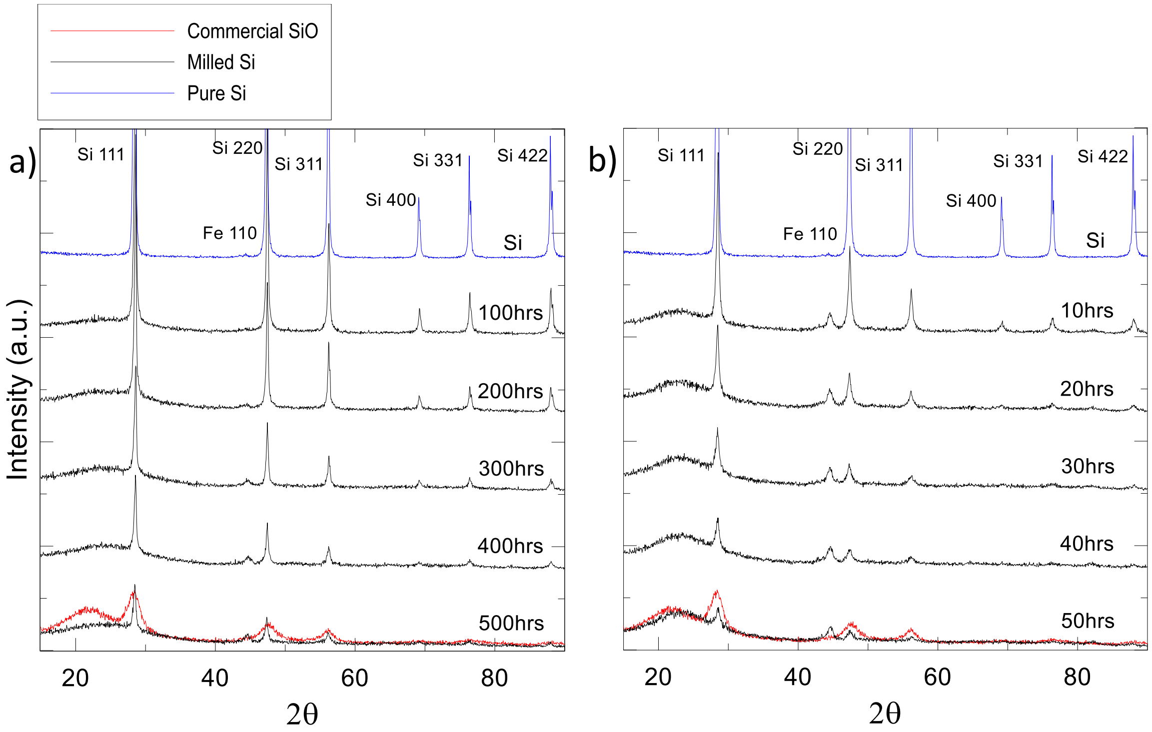

Figure 4-1 - Time dependant XRD patterns of samples taken from, a) Roller Mill and b) Attritor mill showing the effect of total milling time

Figure 4.2 shows the oxygen contents versus time measured by the KOH oxygen determination method described in Chapter 3. Contrary to previous milling attempts[42], it is shown that for either method we have the ability to synthesize SiO_x powder with oxygen content control throughout the electrochemically useful range. For the roller mill method, we have control of oxygen content for $0 \leq x \leq 1.5$, and $0 \leq x \leq 1.7$ for the attritor mill. This presents the ability to tune oxygen content for the correct balance between specific capacity and SiO_2 content to create stabilizing irreversible lithium oxides and lithium silicates.

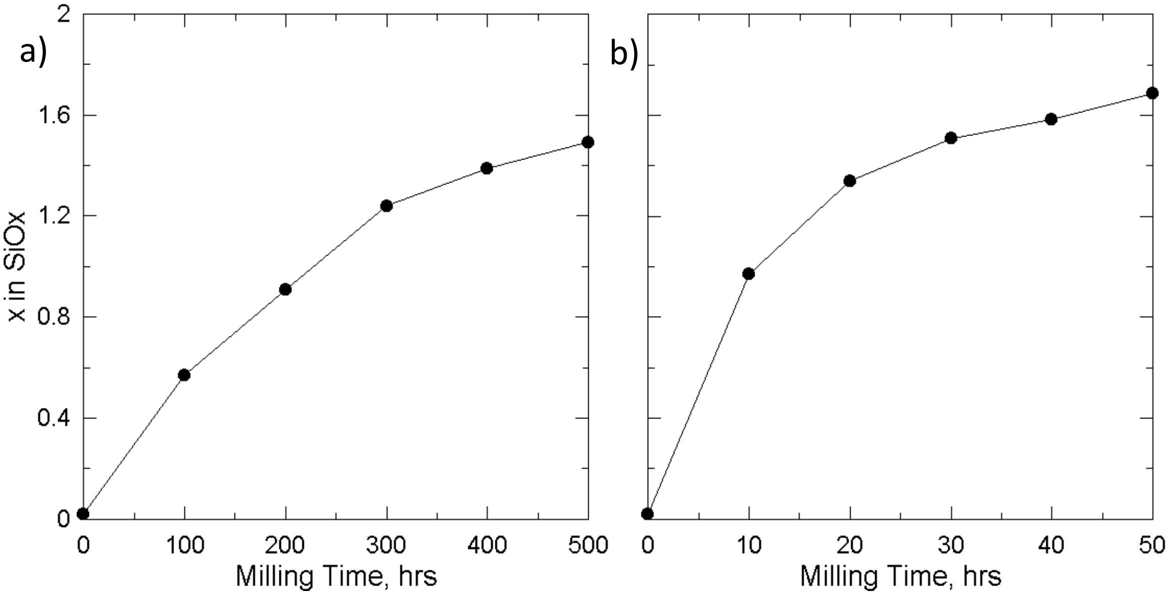

Figure 4-2 - Oxygen content of ball milled silicon samples taken from a) Roller Mill and b) Attritor mill found using the KOH oxygen determination method

Iron contamination in the samples can be seen in the XRD patterns of Figure 4.1. These are evident in both the roller and attritor milling methods. The iron contamination seen in the roller mill samples can be largely reduced by better placement of the internal scraper bar. Evidence for this is provided later. Figure 4.3 shows attritor arm wear contributing to iron contamination shown in the XRD patterns of the attritor mill samples. This is likely due to the aggressive nature of the attritor milling technique running at 700 RPM for 50 hours. Iron contaminations were planned to be quantified through Mossbauer spectroscopy for final targeted oxygen content SiO_x samples used for coin cell testing. However due to Covid-19 restrictions, access to the Mossbauer Spectrometer was not possible.

Figure 4-3 – Evidence of attritor arm wear causing unwanted Fe contamination in the SiO_x powders

4.2 TARGETED OXYGEN CONTENT MILLING

All of the necessary data needed to reach a targeted oxygen content was gathered though the long run milling trials described previously. It was decided that an oxygen content of $x = 0.6$ would offer the appropriate balance between specific capacity and lifetime. This oxygen content was chosen to maximise specific capacity of the material while retaining the stabilizing microstructure observed in the SiO_x particles. Finding the optimal oxygen content is included as future work. To achieve this goal the roller mill was first purged with argon to remove any trapped air in the milling chamber. The mill was then run continuously for 400 hours under argon flow to reduce particle size and crystallinity without adding oxygen content. Oxygen was then introduced at 400 hours with periodic sampling happening every 25 hours to monitor the change of oxygen content. This resulted in a final oxygen content of x = 0.63 as shown in Figure 4.4. The time dependant XRD patterns (Figure 5a) of the roller mill samples show good progression towards a more amorphous structure. Using the Scherrer equation the crystallite size of the silicon regions can be estimated to be approximately 22 nm.

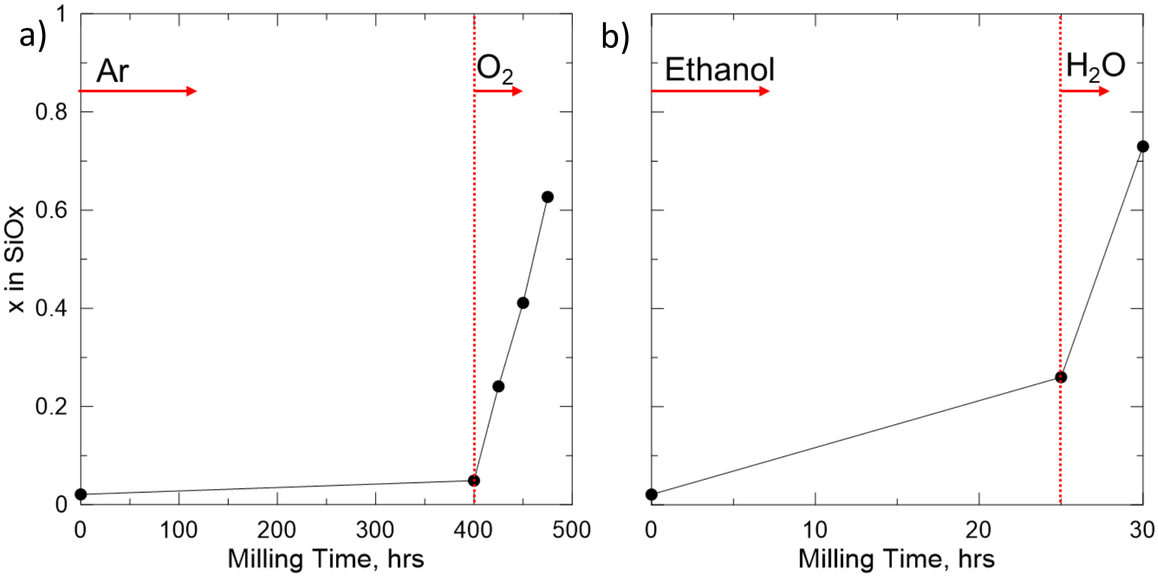

Figure 4-4 - Oxygen content of ball milled silicon as part of targeted oxygen content milling, measured by the KOH method. Samples from a) Roller Mill and b) Attritor mill

For the attritor mill, targeted oxygen content milling was achieved by milling for 25 hours in ethanol, and 5 hours in deionized water. After the first 25 hours, the mill was stopped and the attritor can full of slurry and media was baked in an oven overnight at 95°C. Since this milling process is so short only two samples were taken. One sample after the 25 hours milling in ethanol, and the final removed sample after a further 5 hours in deionized water. The final SiO_x sample was measured to have an oxygen content of x = 0.73 with an estimated silicon crystallite size of ~20 nm. As shown in Figure 4.4b the final oxygen content of the attritor milled SiO_x is slightly higher than expected due to oxygen content gained during milling time in ethanol. It is believed that this can be reduced by removing excess water content present in the ethanol before milling.

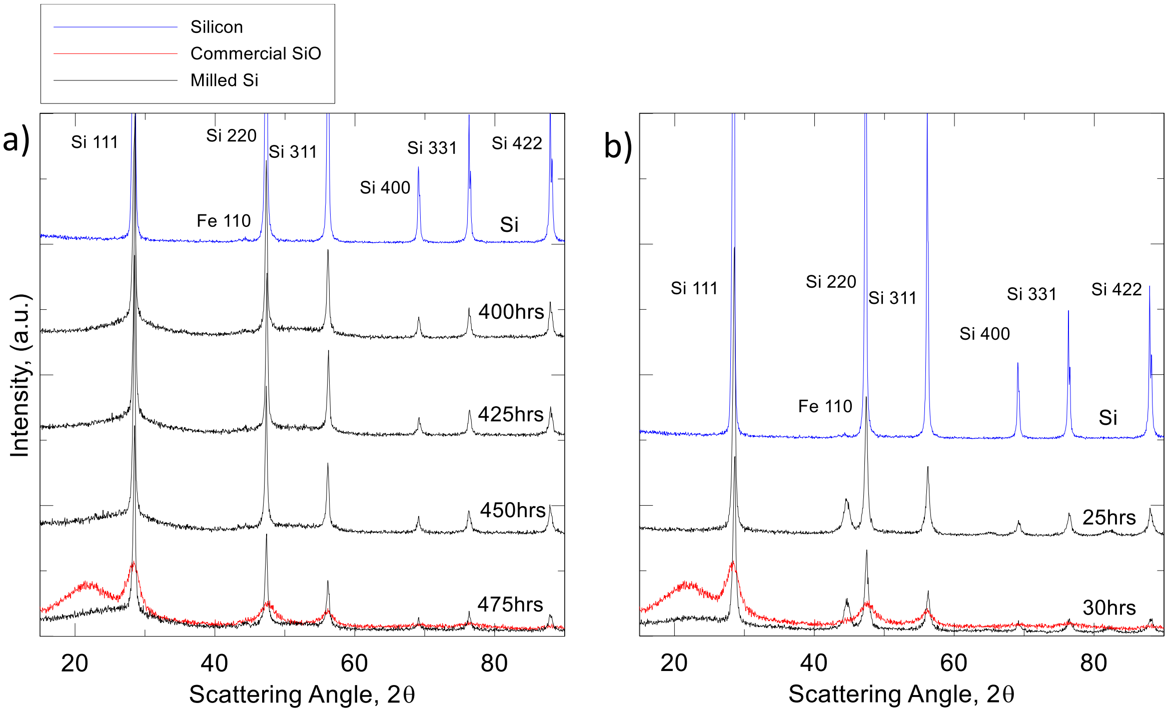

Figure 4-5 – Time dependant XRD patterns of samples taken from, a) Roller mill and b) Attritor mill

BET surface area analysis was done on the samples removed from both the roller mill and the attritor mill at various times. Figure 4.6 shows the negative effects of ball milling causing high surface area powders for use as electrode material. This will be very detrimental to electrode lifetime when used in a lithium-ion cell due to the excessive consumption of electrolyte and active lithium in the formation of the SEI. Figure 4.6 shows a steady increase in surface area as milling time increases. The specific surface area of the base silicon powder used in the mill was measured to be $5.2\ m^2/g$, while the final SiO_x sample synthesized by roller milling showed a specific surface area of $24.3\ m^2/g$. This large increase is in part due to the reduction of particle size of the silicon powder and likely the creation of rough particle surfaces. Attritor mill powders were also measured and exhibit a much higher specific surface area of $47.1\ \mathrm{m^2/g}$. Reduction of this surface area of the milled SiO_x would benefit cell lifetime greatly and is a large part of future work to be done in this area.

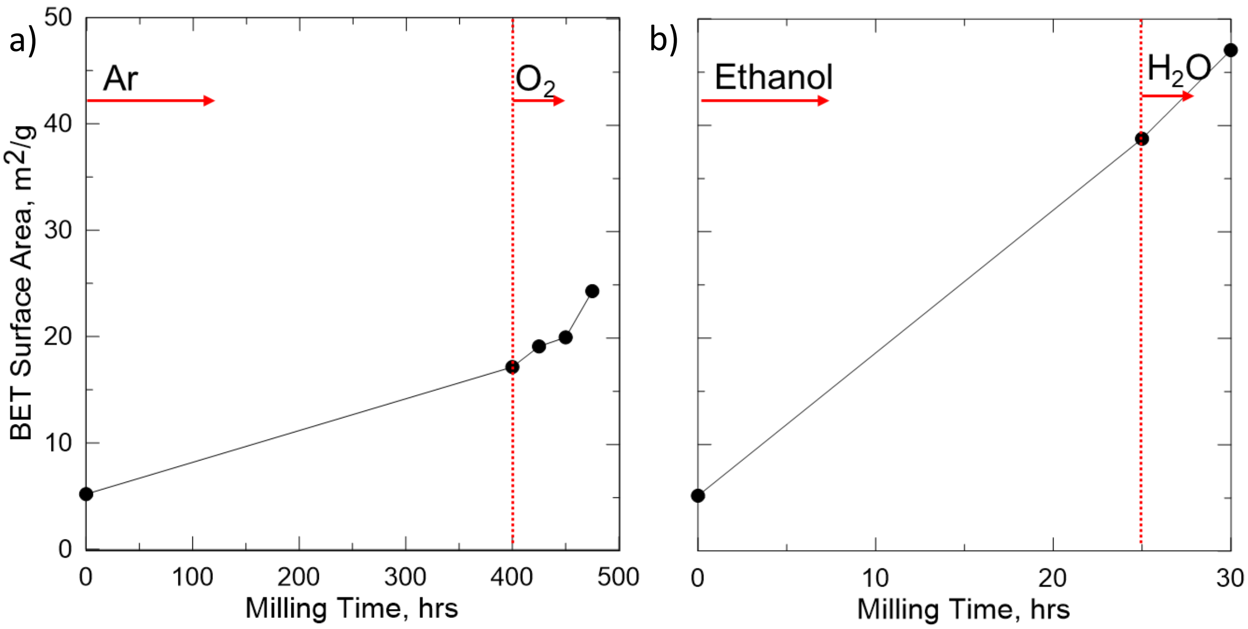

Figure 4-6 - Time dependant BET surface area of samples taken from, a) Roller mill and b) Attritor mill showing the dramatic increase in surface area during milling

Estimating particle size using the specific surface area measurement can be completed using Equation 4.1 assuming spherical particles:

$$d = \frac{6}{S\rho} \qquad \text{E4.1}$$

where d is the diameter of the spherical SiO_x particles, S is the measured BET specific surface area, and ρ is a weighted average density of the given the material composition. Average densities of 2.43 $\mathrm{g/cm^3}$ and 2.45 $\mathrm{g/cm^3}$ were used for the roller mill and attritor mill SiO_x, respectively. These results calculated using Equation 4.1 estimate an average particle diameter of 0.10 μm and 0.05 μm for roller mill and attritor mill powders. The small particle size of the milled powders results in the high specific surface areas measured. This is confirmed through SEM imaging shown in Figure 4-7. The starting silicon powder and the commercial SiO consist of large particles with smooth surfaces. The milled SiO_x consists mainly of submicron particles forming larger aggregates. This morphology makes this material a good candidate for dry particle micro granulation (DPMG) as will be discussed in the future work section.

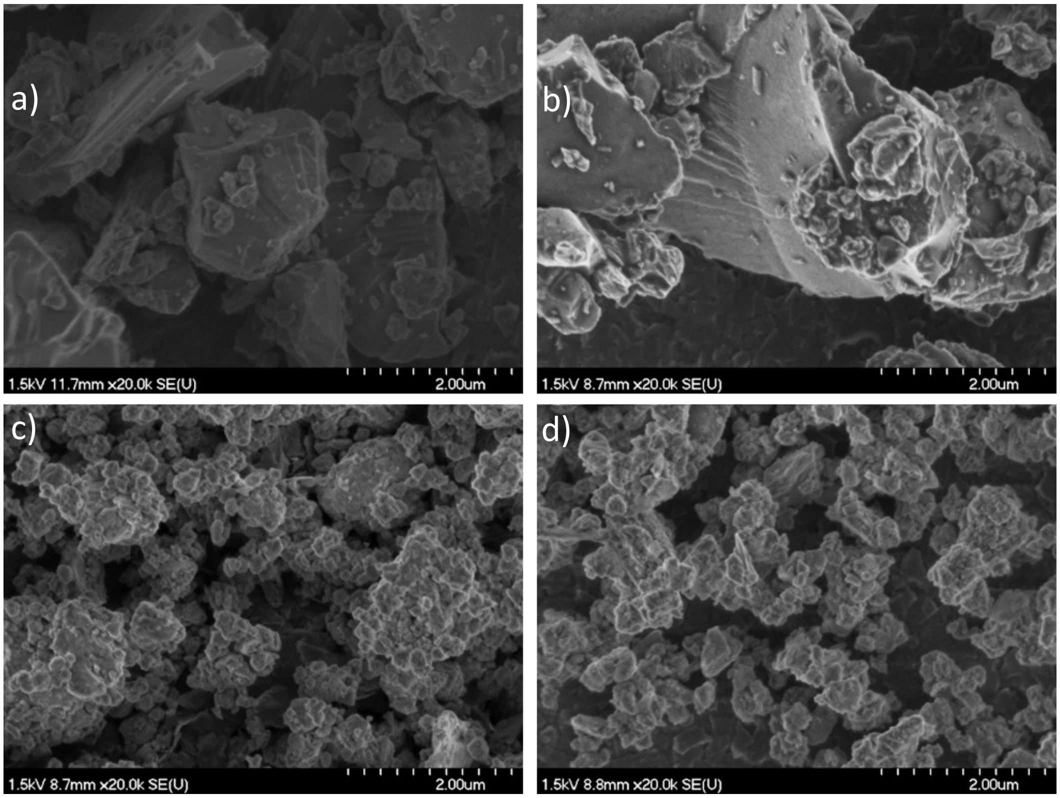

Figure 4-7 - SEM images of a) Silicon starting material, b) Vendor A SiO, c) Roller Mill SiO_x, and d) Attritor Mill SiO_x, comparing particle size and surface morphology

CHAPTER 5 ELECTROCHEMICAL CHARACTERIZATION

Electrochemical testing was completed using lithium foil half cells. Material was mixed with varying amounts of SWCNT, to improve electrode adhesion, reduce loss of electrical contact between active particles, and increase electrical conductivity of the electrode. The improved electrode adhesion is supported by Figure 5.1 that shows the effect of adding SWCNT solution to the electrode slurry resulting in less electrode cracking during preparation. Even as little as 0.15 wt% is enough to make a noticeable improvement.

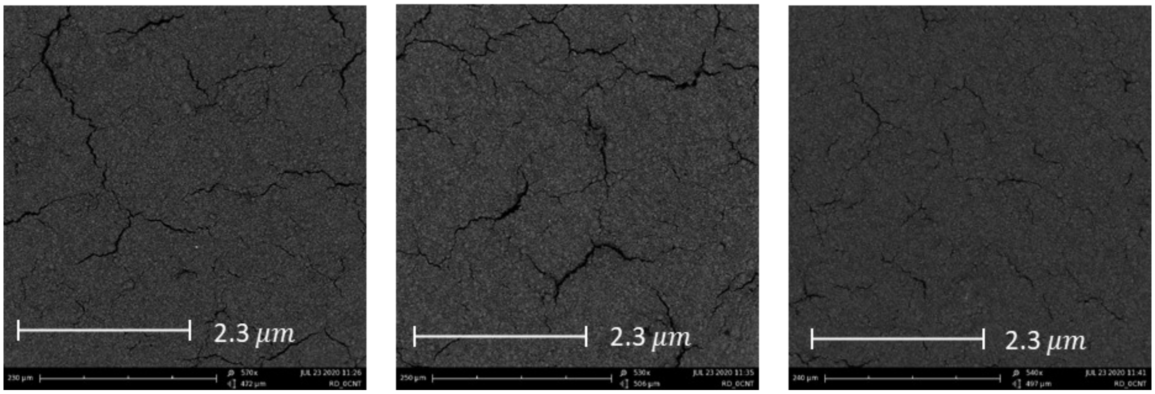

a) b) c)

Figure 5-1 – Benchtop SEM images showing the effectiveness of SWCNT as a binder strengthener in increasing additive amounts of a) 0%, b) 0.08%, c) 0.15%, reducing crack size and length.

5.1 ROLLER MILL SIO$_X$

Figure 5.2 shows half cell cycling results of roller mill SiO$_x$ (where x = 0.63) powders with SWCNT conductive additive. The upward trends of the data as cycling advances suggest possible particle fracturing and exposure of fresh silicon surface previously unreachable due to solid state lithium diffusion limitations. What is shown is an impressive increase in capacity retention during the first full cycle. Each cell containing

SWCNT had much higher first cycle coulombic efficiencies and higher initial specific capacity than the cell without. These cells exhibited first cycle coulombic efficiencies of 73.9%, 74.1%, 74.4% (For 0.1 wt%, 0.2 wt%, and 0.4 wt% SWCNT respectively) versus a lowly 61.7% CE for a cell without SWCNT. This 12% increase can likely be attributed to improved electrical contact between active particles during the first full cycle. It is possible that the string like nature of the SWCNTs help maintain electrical contact during cycling. The noticeable loss of specific capacity from the cell with 0.0 wt% SWCNT during the first cycles results in a more stable CE as cycling proceeds. This may suggest the initial lithiations are where the most electrical disconnections happen and the addition of SWCNT results in high initial capacity retention but slow active particle loss over the full 50 cycles instead. The high surface area of the CNTs contribute to the continual lithium consumption during cycling, as evidenced by the reduced CE of cells using SWCNT compared to the cells without in Figure 5.2.

The cell with 0.1 wt% SWCNT begins to experience accelerated capacity fade after only 10 cycles, whereas the cell with 0.2 wt% does not begin to see accelerated capacity fade until almost 30 cycles. These accelerated capacity fade trends may be the result of loss of electrical contact to some of the SiO_x particles. The cell with 0.4 wt% SWCNTs demonstrates the best cycle retention after 50 cycles of the various compositions tested. This then suggests that SWCNTs should be incorporated into all high volume expansion materials based on their effectiveness in a silicon-based electrode material.

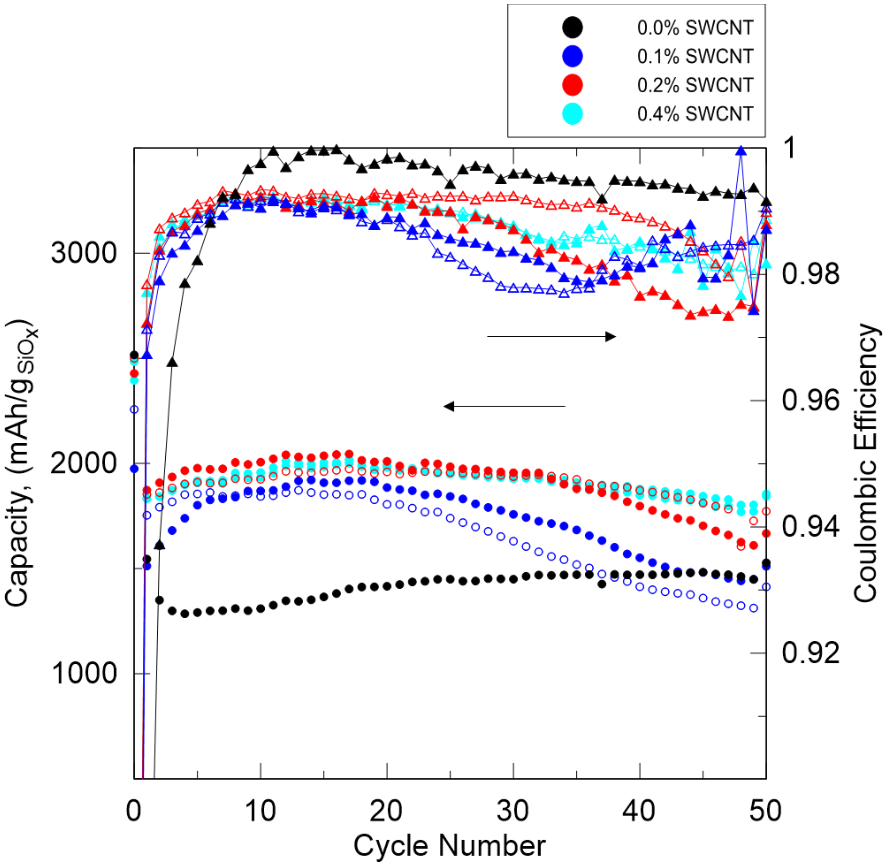

Figure 5-2 – Roller Mill SiO_x cycle life over 50 cycles with varying SWCNT additive

Figure 5.3 shows voltage versus specific capacity data for the roller mill SiO_x (where x = 0.63) powder. Duplicate cells are provided with the open symbols of the same color. From this graph it is easy to see that the addition of SWCNTs in any concentration reduces first cycle irreversible capacity. These V-Q curves also suggest an increase in conductivity when looking at the initial voltage drop when beginning the second lithiation of the electrode. The continuous motion of the voltage vs capacity curves to the right is due to the consumption of active lithium during SEI fracturing and repairing. The increased right shift of cells with high SWCNT addition can be partially attributed to the high surface area of the CNTs causing increased SEI formation. This material shows good reversible capacity of approximately 2000 mAh/g when used in conjunction with a high loading (0.2 wt% to 0.4 wt%) of SWCNT.

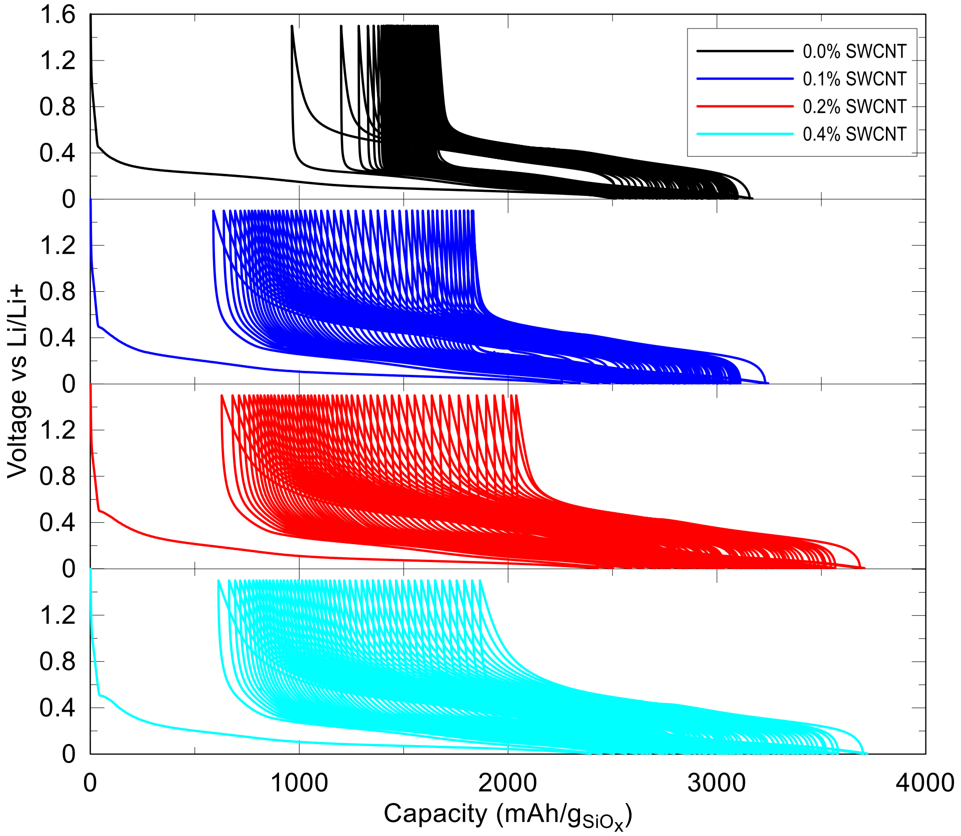

Figure 5-3 – Roller Mill SiO_x V-Q curves over 50 cycles with varying SWCNT additive

5.2 ATTRITOR MILL SiO_x

Figure 5.4 displays cycling data gathered for SiO_x (where x = 0.73) synthesized through attritor milling. Duplicate cells are provided with the open symbols of the same color. This graph clearly shows the performance advantages of using SWCNT additive. The material exhibits a reversible capacity of 1641 mAh/g when used in conjunction with

0.4 wt% SWCNTs. As it did with roller mill SiO_x, the SWCNT additive improved first cycle CE of all cells from 69.7% to 73.1%, 72.4%, and 72.7% for (0.1 wt%, 0.2 wt%, and 0.4 wt% SWCNT). This increase in CE will reduce active lithium consumption during SEI formation that leads to cell failure. As observed in the cells using roller mill SiO_x, the improved first cycle CE as a result of SWCNT addition results in lower CE over the full 50 cycles recorded suggesting active material loss is simply delayed rather than avoided. As a result, cells using higher additions of SWCNT do show lower CE than cells without. The lower CE of the cells using high SWCNT addition can be partially attributed to the high surface area nanotubes causing increased SEI formation during cycling.

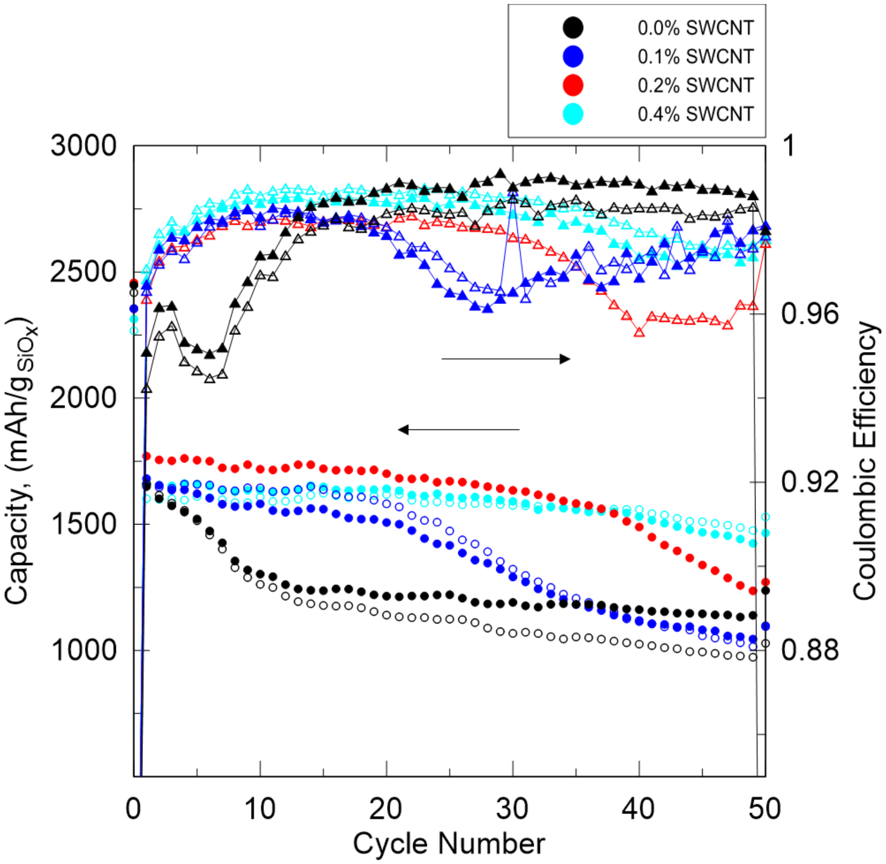

Figure 5-4 – Attritor Mill SiO_x cycle life over 50 cycles with varying amount of SWCNT additive

The addition of SWCNTs also has a clear effect in extending the lifetime of the electrodes. The cell cycling without any SWCNT additive experiences an immediate loss of capacity over the first ten cycles likely due to the collapse of electrode structure and a loss of electrical contact between active particles. The cells with 0.1 wt% and 0.2 wt% SWCNTs experience similar capacity fade after approximately 20 and 40 cycles, respectively. This would support the theory that the CNTs help maintain electrical contact between the electrode and active particles much better than simple carbon black particles.

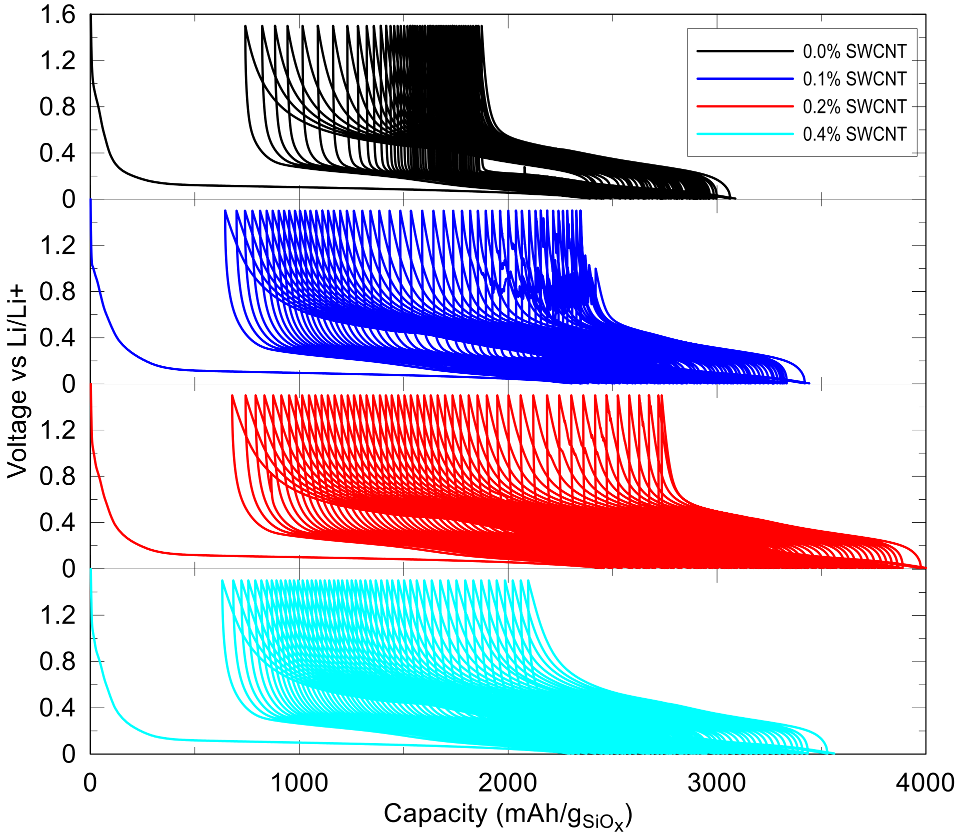

Figure 5-5 – Attritor Mill SiO_x V-Q curves over 50 cycles with varying SWCNT additive

The V-Q data for the attritor mill SiO_x once again shows the benefits of SWCNT in reducing first cycle irreversible capacity. What we can also see is the consistent loss of capacity due to the imperfect coulombic efficiency of the material. This means that on each lithiation some active lithium is being consumed through formation of SEI and is not removed during delithiation. This is possibly linked to the high surface area of the active material and the SWCNTs combined with the high volume expansions experienced during lithiation. A lower surface area material should display better capacity retention with an extended lifetime.

5.3 COMMERCIAL SIO- VENDOR A

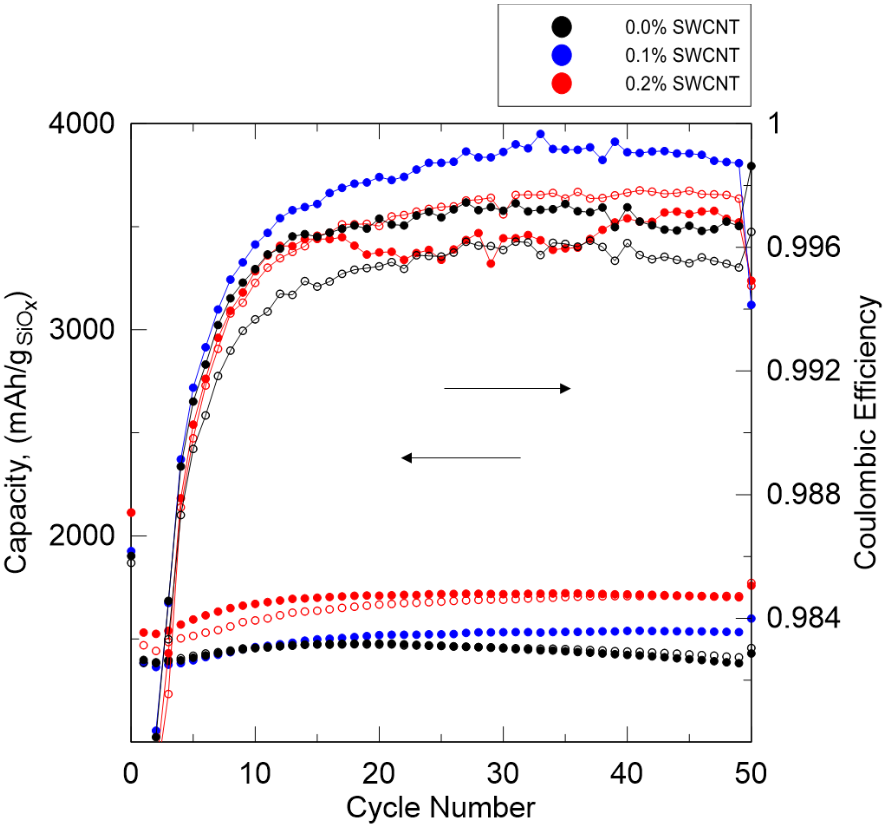

Figure 5-6 – Vendor A SiO cycle life over 50 cycles with varying SWCNT additive

Commercial SiO samples offer great reversible capacity of approximately 1750 mAh/g when used with 0.2 wt% SWCNT. Figure 5.6 shows that the impressive capacity retention of the SiO from vendor A is further improved with addition of SWCNTs. In these cells we see improved first cycle CE and improved cycling CE as a result of SWCNT addition. Duplicate cells are provided with the open symbols of the same color. Since this material already offers good cycle performance, lower concentrations of SWCNTs were added. The SiO from vendor A shows the advantage of low surface area powders as we see less irreversible capacity during each cycle compared to the milled SiO_x showcased previously.

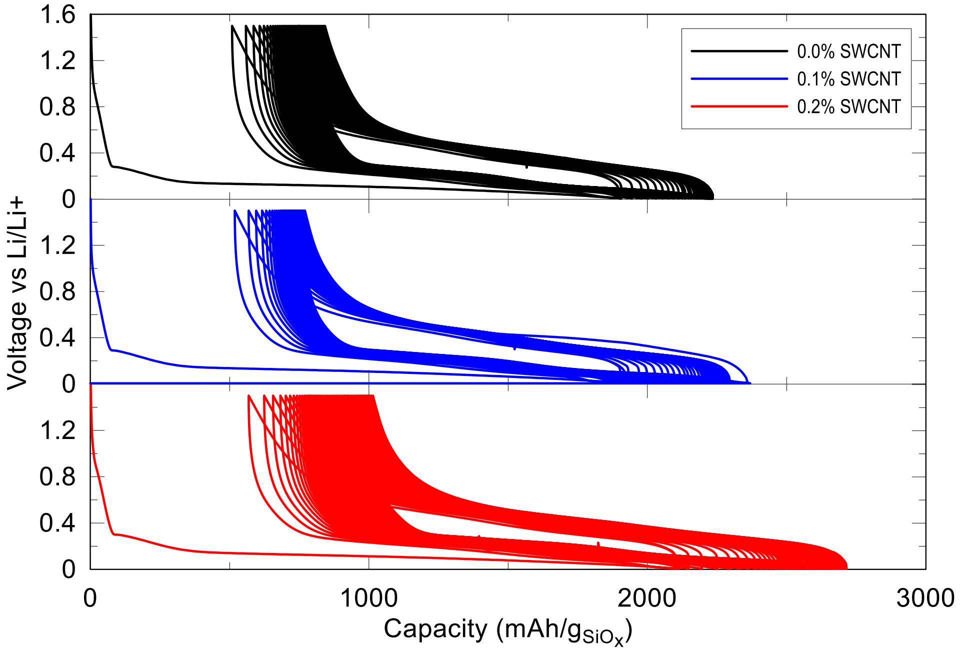

Figure 5-7 – Vendor A SiO V-Q curves over 50 cycles with varying SWCNT additive

5.4 BEST CELL COMPARISONS

The best cells made from the three different materials tested are compiled into single comparison plots. Electrodes used for direct comparisons are the roller mill and attritor mill SiO_x with 0.4 wt% SWCNT, compared to the SiO from vendor A with 0.2 wt% SWCNT. Figure 5.8 shows the roller mill SiO_x cells offer a higher specific capacity than the commercial SiO over 50 cycles, but there is a distinct downward trend showing consistent capacity fade. The higher oxygen content of the attritor mill SiO_x compared to roller mill SiO_x results in a lower reversible specific capacity as more silicon was oxidized and reacted to form supporting lithium silicates and lithium oxides. The lower specific capacity can also be linked to the high amounts of iron contamination within the sample. Attritor mill SiO_x initially offers a higher specific capacity than the vendor A SiO but quickly falls below due to its steady capacity loss thought to be from loss of active particle connection. Beyond 50 cycles it is likely that the vendor A SiO would prove to be the better electrode as the plots show no immediate signs of capacity loss. This is supported by looking at the CE of the electrodes after 50 cycles as the milled SiO_x powders show signs of drastic capacity fade that are not observed in the vendor A SiO cycling data. It is clear from these plots that the SiO_x made by mechanical milling require more work likely into reducing the specific surface area of the material.

Specific surface area of a material becomes important when looking at SEI formation and electrolyte consumption. From the results displayed in Figure 5.9, the high surface area of the attritor mill powder, 47.07 m^2/g, results in a lower coulombic efficiency on every cycle as the volume expansions during lithiation causes SEI fracturing and electrolyte consumption during repair. The SiO_x produced by roller milling experiences this same problem but to a lesser extent with its smaller specific surface area of 24.27 m^2/g. The low surface area of the SiO from vendor A, 1.21 m^2/g, results in an improved coulombic efficiency meaning less active lithium and electrolyte consumption during cycling. When a lithium counter electrode is used this consumption of lithium is not detrimental. If these materials are incorporated into full cells with a limited lithium inventory, then lithium consumption becomes a major source of cell failure.

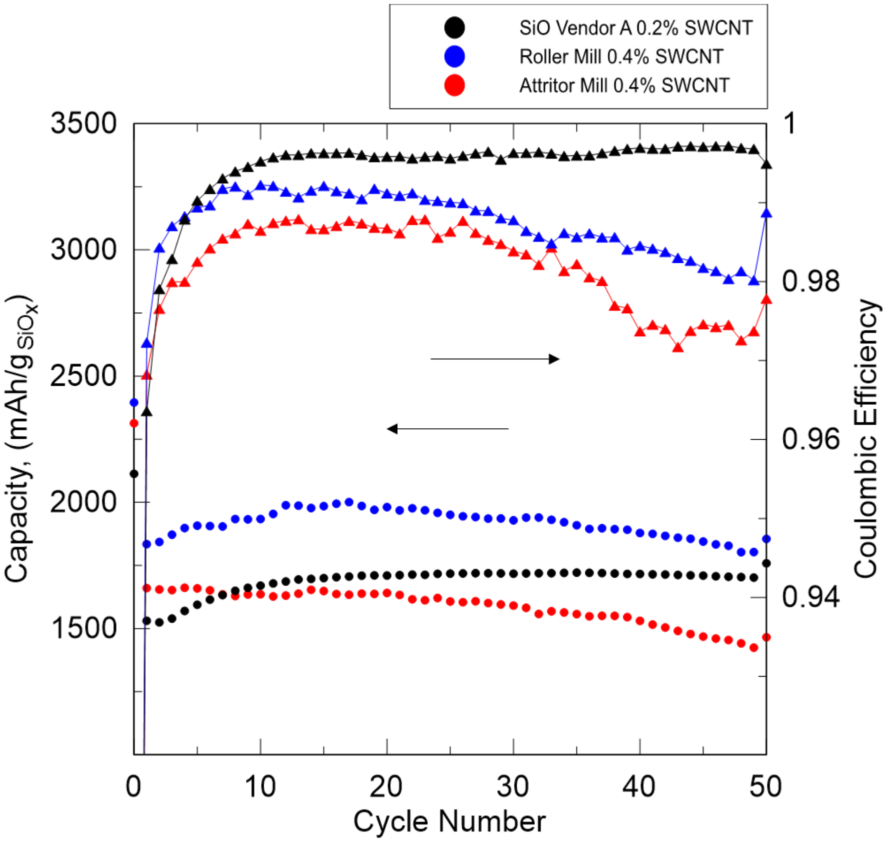

Figure 5-8 – Best cells from milled SiO_x and commercial SiO looking at cycle life over 50 cycles

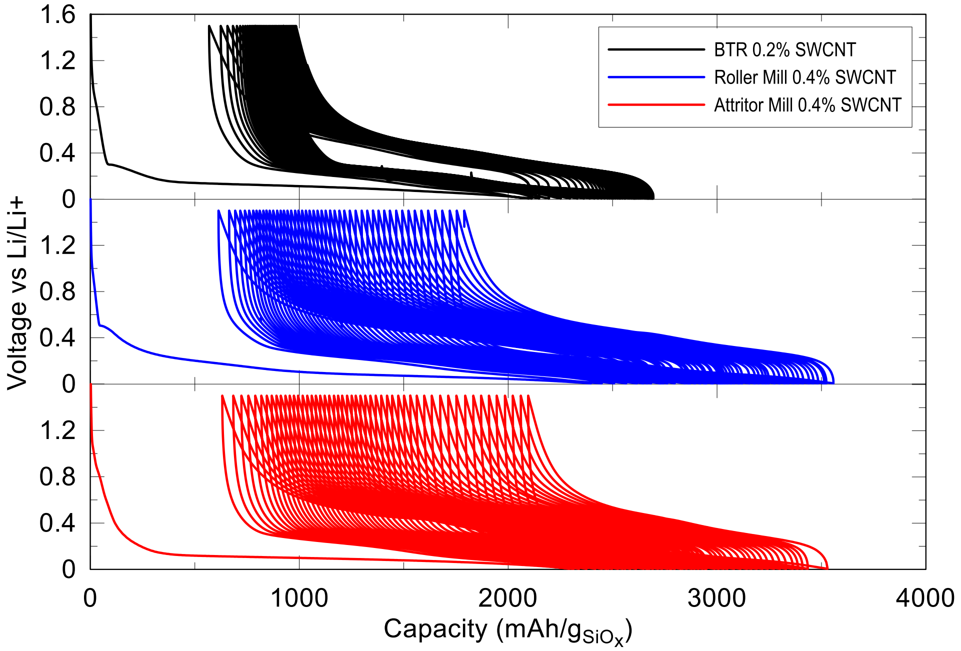

Figure 5-9 – Best cells from milled SiO_x and commercial SiO looking at V-Q curves over 50 cycles

CHAPTER 6 CONCLUSION

6.1 SUMMARY OF RESULTS

The data outlined in this thesis has shown it is possible to synthesize SiO_x for use in lithium-ion batteries using well studied mechanical milling methods. Starting from only silicon powder, milling was used to add oxygen to the silicon with full control of the final oxygen content of the powder. This was done in two milling methods. A horizontal roller mill was specifically modified to mill silicon for long periods of time under oxygen flow causing an oxidizing reaction and mechanical alloying of silicon and silicon dioxide particles. The same mechanical alloying effect was achieved by wet milling powders in an attritor mill using distilled water as the milling solvent. This method utilized the hydrogen producing reaction between silicon and water to oxidize the silicon powder to a controlled amount.

The synthesized powders were characterized with XRD to qualitatively monitor amorphization, iron contamination, and oxygen content. BET surface area analysis was used to measure the increase of the specific surface area with time spent milling. It was found that surface area increases dramatically as milling proceeds and the choice of milling atmosphere or milling solvent has little role in its increase. The oxygen content of the synthesized powders were measured using a technique developed in this work. The molar ratio of Si to SiO_2 is determined by quantifying the amount of hydrogen produced in the reaction between Si and a KOH water solution. This method was used to track oxidation rates and predict milling durations necessary to reach the desired composition.

Data was collected during long run milling trials where the oxidizer was introduced at zero hours of milling. This crucial data was then used to determine total milling times and the time spent milling in an oxidizing environment required to reach a targeted oxygen content. An oxygen content of SiO_x where $x = 0.6$ was chosen as the target as it was predicted to offer a high specific capacity while incorporating a high amount of particle stabilizing SiO_2 regions.

The targeted oxygen content materials were then incorporated into lithium half cells while testing a SWCNT conductive additive. The prepared materials offered large specific capacities and are comparable to commercial SiO synthesized through vapor deposition. Using the SWCNT conductive additive, cycle life is dramatically improved and demonstrates cycle life comparable to commercial materials. The high surface areas of the milled SiO_x material result in consistent active lithium consumption through fracturing and repairing of the anode SEI. This will also result in electrolyte consumption that can be directly related to cell failure.

The work presented in this thesis shows the effectiveness of synthesizing SiO_x through mechanical milling. There are several areas of improvement that need to be further investigated.

6.2 FUTURE WORK

A method that did not undergo any investigation is the differences caused by changing the time when the oxygen content is introduced, either as oxygen gas flow or distilled water milling solvent. Currently, oxygen or distilled water are introduced after many hours of particle size reduction and amorphization caused by milling. An area of interest is to study the effect of introducing the oxidizer early in the process, or periodically over the course of the total milling time. Early introduction of oxygen content would allow more time for the milling process to create a homogeneous combination of Si and SiO_2 regions and therefore a more structurally stable microstructure beneficial to electrochemical cycling. Comparing these methods using coin cells and imaging methods such as TEM would help the fundamental understanding of the enhanced cycling stability.

It is believed that the largest problem that exists with the mechanically milled SiO_x is the large specific surface area that results from the repeated fracturing and recombining. These large surface areas result in accelerated capacity fade due to electrolyte consumption through continuous SEI formation. Difficulties are also experienced during electrode preparation as the prepared slurry turns into a highly viscous gel. This is attributed to the high surface area and the effects of unwanted silicon oxidation during slurry mixing. To simply reduce the surface area, the final powder could be classified to only include particles of sufficient size. To decrease surface area and eliminate wasted powder from classifying, Obrovac et al developed a technique using mechanofusion processing that they call dry particle microgranulation.[75] With this method of granulation, sub micron particles could be recombined to form larger secondary particles. This method involves the use of smooth ZrO_2 'template particles' that accumulate the sub micron sized 'feed particles' into large aggregates while undergoing mechanofusion. The Dahn lab has the equipment needed for this work. This method has been shown to reduce surface area of ball milled graphite and NMC material while forming uniform 25 micron particles starting from sub micron feed particles and 50 micron ZrO_2 template particles. Application to ball milled SiO_x would greatly improve long term performance and usability of the material. A final material that does not require special processing is more desirable to industrial applications.

A targeted oxygen content of x = 0.6 for the final SiO_x samples was chosen to maximize specific capacity while assuming it incorporates enough SiO_2 regions to form the supporting structure of irreversible Li_4SiO_4 and Li_2O. To back up this claim, a variety of samples ranging from x = 0 to x = 1 should be made in to develop a data set that can be used to optimize the balance between specific capacity and lifetime. Work much like that done by Al-Maghrabi et al. on sputtered SiO_x would be beneficial to understanding the role of SiO_2 regions within the electrode.[41] This data could then also be used to tailor the material for applications that may value characteristics of battery longevity over charge capacity.

Mossbauer spectroscopy can be used to identify material compositions not detectable in measurements such as XRD. Following methods described by Scott et al., Mossbauer spectroscopy can be used quantitatively to determine Fe contamination within milled SiO_x powders.[69] Measurements of this type were slated to take place but limited availability of spectrometer time and reduced access to labs during Covid-19 meant this did not occur in time for inclusion.

The methods presented in this thesis are a response to the difficulties that arise when trying to produce SiO by vapor deposition on an industrial scale. The precise heat and vacuum control needed to produce the correct SiO variation does not translate well to mass volume production. Using a well-known industrial process such as ball milling offers the ability to produce the material in a scalable and industrial process. Now a company called 6K is using microwave based plasma technology to synthesize material in a high speed continuous flow operation.[76] This method produces multiphase composite materials directly from a solution in a fast pyrolysis method. Homogeneous precursor solution is formed into precise droplets and injected into the microwave plasma to undergo rapid heating followed by evaporation, thermal dissociation, and recondensation in a matter of milliseconds to form ultrafine particles.[77] In the formation of silica nano particles, solutions containing $SiCl_4$ or $Si(OC_2H_5)_4$ are injected into oxygen or air heated to 5000K through microwave irradiation.[77] The advantages of synthesis through plasma processing make it a desirable method and it will be important to test its electrochemical properties in comparison to ball milled SiO and SiO by vapor deposition.

Current batteries on the commercial market do not use a full Si alloying negative electrode. The lithium alloy negative electrodes are blended into a mostly graphite electrode in an effort to increase specific capacity without lowering cycle life.[33] An important area of study would be incorporating the milled SiO_x into a graphite electrode at various percentages ranging from full SiO_x to full graphite electrodes and conducting cell lifetime studies. Along with this would be incorporation of much higher percentages of SWCNTs as its effectiveness has been demonstrated clearly in Chapter 5. The results of this work would demonstrate the relation between the three factors of SiO_x doping, specific capacity, and cell lifetime. Depth of discharge studies would be an important area of study as this would reflect real world usage better than full charge discharge cycling.

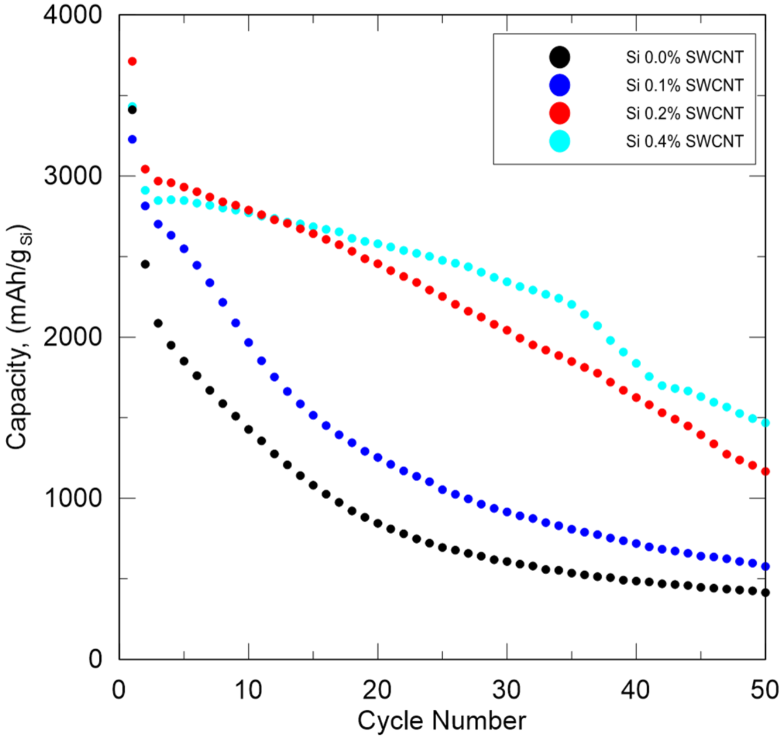

Figure 6-1 – Si cycling data with varied amounts of SWCNT additive

The effectiveness of OCSiAl SWCNT in stabilizing the milled SiO_x and the commercial SiO has reintroduced the idea of using pure Si without oxides or composite supporting structures. With electrode structure collapse and the electrical disconnection of active particles being the main reason for electrode capacity loss and eventual failure; the use of good CNTs combined with a highly elastic polymer binder could be hugely beneficial to electrode lifetime. Early work shown in Figure 6.1 shows the effect of adding up to 0.4 wt% SWCNT to a standard Si electrode. Continuation of this work will be incorporating more SWCNT in place of the 10 wt% conducting carbon in the electrode. The string like nature of the nanotubes will help maintain electrical contact with all active particles in the electrode much better than single carbon particles. Work surrounding optimizing Si lithiation cut off points should be conducted now using SWCNTs to show the best performance of the Si electrodes.[25]

As previously mentioned, Si is consistently combined with graphite electrodes as a way to increase capacity of the electrode.[26,27,29] Work is needed to be done in this area to find the correct ratio of graphite and silicon within the electrode. This would be completed using a high percentage of SWCNT as their effectiveness has been repeatedly presented in this thesis.

REFERENCES

1. M. Genovese, A. J. Louli, R. Weber, S. Hames, and J. R. Dahn, *J. Electrochem. Soc.*, **165**, A3321–A3325 (2018).

2. A. J. Louli, M. Genovese, R. Weber, S. G. Hames, E. R. Logan, and J. R. Dahn, *J. Electrochem. Soc.*, **166**, A1291–A1299 (2019).

3. J. R. Dahn, T. Zheng, Y. Liu, and J. S. Xue, *Science (80-.).*, **270**, 590–593 (1995).

4. R. Fong, U. von Sacken, and J. R. Dahn, *J. Electrochem. Soc.*, **137**, 2009–2013 (1990).

5. C. Wang, A. J. Appleby, and F. E. Little, *J. Electroanal. Chem.*, **519**, 9–17 (2002).

6. J. E. Harlow, X. Ma, J. Li, E. Logan, Y. Liu, N. Zhang, L. Ma, S. L. Glazier, M. M. E. Cormier, M. Genovese, S. Buteau, A. Cameron, J. E. Stark, and J. R. Dahn, *J. Electrochem. Soc.*, **166**, A3031–A3044 (2019).

7. M. N. Obrovac and V. L. Chevrier, *Chem. Rev.*, **114**, 11444–11502 (2014).

8. J. R. Dahn, W. Xing, and Y. Gao, *Carbon N. Y.*, **35**, 825–830 (1997).

9. M. Winter, J. O. Besenhard, M. E. Spahr, and P. Novak, *Adv. Mater.*, **10**, 725–763 (1998).

10. X. Bai, T. Li, and Y. J. Bai, *Dalt. Trans.*, **49**, 10003–10010 (2020).

11. J. H. Seo, K. Verlinde, R. Rajagopalan, E. D. Gomez, T. E. Mallouk, and C. A. Randall, *Mater. Sci. Eng. B Solid-State Mater. Adv. Technol.*, **250**, 114435 (2019) https://doi.org/10.1016/j.mseb.2019.114435.

12. M. N. Obrovac, L. Christensen, D. B. Le, and J. R. Dahn, *J. Electrochem. Soc.*, **154**, A849 (2007).

13. Y. Oumellal, N. Delpuech, D. Mazouzi, N. Dupré, J. Gaubicher, P. Moreau, P. Soudan, B. Lestriez, and D. Guyomard, *J. Mater. Chem.*, **21**, 6201–6208 (2011).

14. X. Zuo, J. Zhu, P. Müller-Buschbaum, and Y. J. Cheng, *Nano Energy*, **31**, 113–143 (2017) http://dx.doi.org/10.1016/j.nanoen.2016.11.013.

15. J. H. Ryu, J. W. Kim, Y. E. Sung, and S. M. Oh, *Electrochem. Solid-State Lett.*, **7** (2004).

16. E. Peled, *J. Electrochem. Soc.*, **126**, 2047–2051 (1979).

17. A. J. Smith, J. C. Burns, X. Zhao, D. Xiong, and J. R. Dahn, *J. Electrochem. Soc.*, **158**, A447 (2011).

18. M. Nie, D. Chalasani, D. P. Abraham, Y. Chen, A. Bose, and B. L. Lucht, *J. Phys. Chem. C*, **117**, 1257–1267 (2013).

19. P. Verma, P. Maire, and P. Novák, *Electrochim. Acta*, **55**, 6332–6341 (2010) http://dx.doi.org/10.1016/j.electacta.2010.05.072.

20. E. Peled, D. Golodnitsky, and G. Ardel, *J. Electrochem. Soc.*, **144**, L208–L210 (1997).

21. K. R. Lawless, *Reports Prog. Phys.*, **37**, 231–316 (1974).

22. N. N. Sinha, J. C. Burns, and J. R. Dahn, *J. Electrochem. Soc.*, **160**, A709–A714 (2013).

23. D. Aurbach, *J. Power Sources*, **89**, 206–218 (2000).

24. T. Utsunomiya, O. Hatozaki, N. Yoshimoto, M. Egashira, and M. Morita, *J. Power Sources*, **196**, 8598–8603 (2011) http://dx.doi.org/10.1016/j.jpowsour.2011.05.066.

25. M. N. Obrovac and L. J. Krause, *J. Electrochem. Soc.*, **154**, A103 (2007).

26. J. H. Lee, W. J. Kim, J. Y. Kim, S. H. Lim, and S. M. Lee, *J. Power Sources*, **176**, 353–358 (2008).

27. S. Chae, N. Kim, J. Ma, J. Cho, and M. Ko, *Adv. Energy Mater.*, **7** (2017).

28. R. Petibon, V. L. Chevrier, C. P. Aiken, D. S. Hall, S. R. Hyatt, R. Shunmugasundaram, and J. R. Dahn, *J. Electrochem. Soc.*, **163**, A1146–A1156 (2016).

29. C. H. Yim, F. M. Courtel, and Y. Abu-Lebdeh, *J. Mater. Chem. A*, **1**, 8234–8243 (2013).

30. J. R. Dahn and G. M. Ehrlich, *Linden's Handbook of Batteries* T. B. Reddy and D. Linden, Editors, 4th ed., McGraw Hill Professional, New York, (2011).

31. K. P. C. Yao, J. S. Okasinski, K. Kalaga, J. D. Almer, and D. P. Abraham, *Adv. Energy Mater.*, **9**, 1–7 (2019).

32. M. Wetjen, S. Solchenbach, D. Pritzl, J. Hou, V. Tileli, and H. A. Gasteiger, *J. Electrochem. Soc.*, **165**, A1503–A1514 (2018).

33. J. Kirner, Y. Qin, L. Zhang, A. Jansen, and W. Lu, *J. Power Sources*, **450**, 227711 (2020) https://doi.org/10.1016/j.jpowsour.2020.227711.

34. A. Hohl, T. Wieder, P. A. Van Aken, T. E. Weirich, G. Denninger, M. Vidal, S. Oswald, C. Deneke, J. Mayer, and H. Fuess, *J. Non. Cryst. Solids*, **320**, 255–280 (2003).

35. T. Chen, J. Wu, Q. Zhang, and X. Su, *J. Power Sources*, **363**, 126–144 (2017).

36. S. C. Jung, H. J. Kim, J. H. Kim, and Y. K. Han, *J. Phys. Chem. C*, **120**, 886–892 (2016).

37. Q. Huang, J. Song, Y. Gao, D. Wang, S. Liu, S. Peng, C. Usher, A. Goliaszewski, and D. Wang, *Nat. Commun.*, **10**, 1–7 (2019) http://dx.doi.org/10.1038/s41467-019-13434-5.

38. S. Komaba, K. Shimomura, N. Yabuuchi, T. Ozeki, H. Yui, and K. Konno, *J. Phys. Chem. C*, **115**, 13487–13495 (2011).

39. Q. Pan, P. Zuo, T. Mu, C. Du, X. Cheng, Y. Ma, Y. Gao, and G. Yin, *J. Power Sources*, **347**, 170–177 (2017) http://dx.doi.org/10.1016/j.jpowsour.2017.02.061.

40. H. Yamamura, K. Nobuhara, S. Nakanishi, H. Iba, and S. Okada, *J. Ceram. Soc. Japan*, **119**, 855–860 (2011).

41. M. A. Al-Maghrabi, J. Suzuki, R. J. Sanderson, V. L. Chevrier, R. A. Dunlap, and J. R. Dahn, *J. Electrochem. Soc.*, **160**, A1587–A1593 (2013).

42. Y. Cao, J. C. Bennett, R. A. Dunlap, and M. N. Obrovac, *Chem. Mater.*, **30**, 7418–7422 (2018).

43. M. Hoch and H. L. Johnston, *J. Am. Chem. Soc.*, **75**, 5224–5225 (1953).

44. G. W. Brady, *J. Phys. Chem.*, **63**, 1119–1120 (1959).

45. K. Schulmeister and W. Mader, *J. Non. Cryst. Solids*, **320**, 143–150 (2003).

46. K. Kashiwagi, Y. Yoshida, and Y. Murayama, *Jpn. J. Appl. Phys.*, **30**, 1803–1807 (1991).

47. P. G. Pai, S. S. Chao, Y. Takagi, and G. Lucovsky, *J. Vac. Sci. Technol. A Vacuum, Surfaces, Film.*, **4**, 689–694 (1986).

48. E. Gaffet, F. Bernard, J. C. Niepce, F. Charlot, C. Gras, G. Le Caër, J. L. Guichard, P. Delcroix, A. Mocellin, and O. Tillement, *J. Mater. Chem.*, **9**, 305–314 (1999).

49. J. S. Benjamin, *Metall. Trans.*, **1**, 2943–2951 (1970).

50. I. J. Lin, *J. Therm. Anal. Calorim.*, **52**, 453–461 (1998).

51. V. V Boldyrev, *Russ. Chem. Rev.*, **75**, 177–189 (2006).

52. G. B. Schaffer and P. G. McCormick, *Metall. Trans. A*, **21**, 2789–2794 (1990).

53. E. Gaffet and M. Harmelin, *J. Less-Common Met.*, **157**, 201–222 (1990).

54. Y. Chen, M. Bibole, R. Le Hazif, and G. Martin, *Phys. Rev. B*, **48**, 14–21 (1993).

55. M. Abdellaoui and E. Gaffet, *Acta Mater.*, **44**, 725–734 (1996).

56. C. Aguilar, S. Ordóñez, J. Marín, F. Castro, and V. Martínez, *Mater. Sci. Eng. A*, **464**, 288–294 (2007).

57. M. Krasnowski and T. Kulik, *Mater. Chem. Phys.*, **116**, 631–637 (2009).

58. K. Fumiyoshi Nagao, *United States Pat. US 7744027*, **1**, 1–29 (2010).

59. W. T. Kwon, S. R. Kim, Y. H. Kim, Y. J. Lee, D. G. Shin, J. Y. Won, and S. C. Oh, *J. Korean Ceram. Soc.*, **51**, 121–126 (2014).

60. S. C. Hou, Y. F. Su, C. C. Chang, C. W. Hu, T. Y. Chen, S. M. Yang, and J. L. Huang, *J. Power Sources*, **349**, 111–120 (2017) http://dx.doi.org/10.1016/j.jpowsour.2017.03.024.

61. N. W. Ashcroft and N. D. Mermin, *Solid State Physics*, Saunders College, Philadelphia, (1976).

62. J. I. Langford and A. J. C. Wilson, *J. Appl. Crystallogr.*, **11**, 102–113 (1978) https://doi.org/10.1107/S0021889878012844.

63. L. Russo, F. Colangelo, R. Cioffi, I. Rea, and L. De Stefano, *Materials (Basel).*, **4**, 1023–1033 (2011).

64. B. D. Cullity, *Elements of X-ray Diffraction*, p. 32–106, Addison and Wesley Publishing Company Inc, Reading, US, (1978).

65. *Micromeritics Flowsorb II 2300 Operation Manual*, Norcross, GA, (1990).

66. T. C. Gibb, *Principles of Mössbauer spectroscopy*, Springer, (2013).

67. N. N. Greenwood and T. C. Gibb, *Mossbauer Spectroscopy*, 1st ed., Chapman and Hall Ltd., London, (1971).

68. M. Sorescu, *Mater. Lett.*, **54**, 256–259 (2002).

69. B. Scott, C. A. M. Brown, R. A. Dunlap, and M. N. Obrovac, *MRS Commun.*, **10**, 123–128 (2020).

70. J. M. Tarascon, A. S. Gozdz, C. Schmutz, F. Shokoohi, and P. C. Warren, *Solid State Ionics*, **86–88**, 49–54 (1996).

71. G. Stingeder, S. Gara, S. Pahlke, H. Schwenk, E. Guerrero, and M. Grasserbauer, *Fresenius' Zeitschrift für Anal. Chemie*, **333**, 576–582 (1989).

72. C. P. Aiken, J. Xia, D. Y. Wang, D. A. Stevens, S. Trussler, and J. R. Dahn, *J. Electrochem. Soc.*, **161**, A1548–A1554 (2014).

73. Archimedes of Syracuse, *On Floating Objects*, (c. 250 BCE).

74. S. Put, D. Van Genecheten, and J. S. Bridel, *Int. Pat. Publ. WO 2016/174023 Al* (2016).

75. M. N. Obrovac, L. Zheng, and M. D. L. Garayt, *Cell Reports Phys. Sci.*, **1**, 100063 (2020).

76. M. Edjdal and K. Hadidi, (2016).

77. J. L. H. Chau and C. C. Kao, *J. Non. Cryst. Solids*, **355**, 2448–2450 (2009) http://dx.doi.org/10.1016/j.jnoncrysol.2009.08.023.